Free gas accumulations in basal shear zones of mass-transport deposits (Pearl River Mouth Basin, South China Sea): An important geohazard on continental slope basins

Qiliang Sun[a,b,*], Tiago Alves[c], Xinong Xie[a,b], Jiaxiong He[d*], Wei Li[e], Xianglong Ni[f]

[a]*Key Laboratory of Tectonics and Petroleum Resources, China University of Geosciences, Wuhan 430074, China;*

[b]*College of Marine Science and Technology, China University of Geosciences, Wuhan 430074, China;*

[c]*3D Seismic Lab, School of Earth and Ocean Sciences, Cardiff University, Main Building, Park Place, Cardiff CF10 3AT, United Kingdom;*

[d]*CAS Key Laboratory of Marginal Sea Geology, Guangzhou Institute of Geochemistry, Chinese Academy of Sciences, Guangzhou 510640, China;*

[e]*Institute of Geosciences, University of Kiel, Kiel 24118, Germany;*

[f] *Research Institute of Petroleum Exploration & Development - Northwest (NWGI), Petrochina, Lanzhou 730020*

Abstract

Free gas is an important trigger of instability on continental slopes, and resulting mass-wasting strata can potentially form competent seals to hydrocarbon accumulations. This work uses two high-quality 3D seismic volumes to investigate fluid accumulations at the base of mass-transport deposits in the Pearl River Mouth Basin, South China Sea. In parallel, IODP/ODP borehole data are used to document the petrophysical character of mass-transport deposits formed in similar continental-slope environments to the South China Sea. The interpreted data show gas accumulations as comprising enhanced seismic reflections that are discordant, or vertically stacked, below mass-transport deposits with chaotic seismic facies. Gas was accumulated in basal shear zones of mass-transport deposits in response to differences in capillary pressure and porosity. Free gas in Zone A covers an area of at least 18 km^2. In Zone B, the free gas is sub-circular in plan view and covers an area of 30.58 km^2 for a volume of sediment approaching 1.5 km^3. This work is important as it shows that vertical migration of gas is not significant in mass-transport deposits from the Pearl River Mouth Basin, but up-dip migration along their basal shear zones is suggested in multiple locations. As a result, free gas can pinch-out laterally to extend 1-2 km beyond these same basal shear zones. As a corollary, we show that free gas accumulations below mass-transport deposits comprise an important geohazard and should be taken into account when drilling continental-slope successions in both the South China Sea and continental margins recording important mass wasting. Strata charged with free gas form weak layers, hinting at a novel trigger of retrogressive slope failure on continental slopes worldwide.

Keywords: South China Sea, fluid migration, free gas, mass-transport deposits, seal units, geohazards.

[*]Corresponding author: Dr. Qiliang Sun and Dr. Jiaxiong He
E-mail address: sunqiliang@cug.edu.cn; Hejx@gig.ac.cn.

1. Introduction

Mass-transport deposits (MTDs) can shape both passive and active continental margins, transporting large volumes of sediment to continental-slope basins (e.g. Haflidason et al., 2004; Alves et al., 2009; Alves, 2010; Soares et al., 2012). They are of recognised importance as local geohazards when drilling (e.g. Varnes, 1978; Locat and Lee, 2002; Krastel et al., 2006; Masson et al., 2006; Lo Iacono et al. 2012), and originate when downslope-directed forces exceed resisting forces on a continental slope (e.g. Hampton et al., 1996; Masson et al., 2006; Dugan, 2012). Multiple factors such as high sedimentation rates (e.g., Dalla Valle et al., 2013; Noda et al., 2013), methane hydrate dissociation (e.g., Laberg and Vorren, 2000; Maslin et al., 2005), release of free gas (e.g., Bünz et al., 2005; Best et al., 2003; Dugan and Flemings, 2000), tectonic activity (e.g., Hance, 2003; Chadwick et al., 2012; Laberg et al., 2014), and slope oversteepening (e.g., Strozyk et al., 2010; Ikari et al., 2011) comprise important triggers for the generation of MTDs. In parallel, submarine creep zones act as a precursor of large-scale slope failure (Li et al., 2016).

Failed strata are transported downslope along a basal shear zone of variable thickness and lithology when submarine slope instabilities occur (Alves and Lourenço, 2010). As a result, three distinct domains are identified within MTDs based on their deformation styles (Martinsen, 1994; Lastras et al., 2002; Bull et al., 2009). They are: a) a headwall domain characterised by extensional deformation, including headwall scarps, extensional ridges and blocks; b) a translational domain comprising the main translated body of the MTD (including sidewall scarps, strike-slip deformation, ramps and flats, grooves and striations, blocks, slump folds, longitudinal shears and secondary flow fabrics), and c) a toe domain dominated by compressional deformation, including pressure ridges, small-scale folds and thrusts (Prior et al., 1984; Bull et al., 2009). Outcrop data from SE Crete has shown that glide planes of submarine landslides comprise a deformation zone in which strata is deformed, sheared and fractures to enhance porosity and fluid migration (e.g. Alves and Lourenço, 2010). Importantly, large volumes of fluids can be focused in vertical and horizontal surfaces within, or immediately below displaced blocks and MTDs, with these same blocks marking the sudden release of overburden pressure near the seafloor (Sultan et al., 2004; Flemings et al., 2008; Alves, 2015). Notwithstanding this work, the roles of MTDs on fluid migration after their emplacement have seldom been addressed in the published literature.

In the Pearl River Mouth Basin, small-scale MTDs are observed on a canyon-incised continental slope (e.g. Dickinson et al., 2012; Gong et al., 2013; He et al., 2014; Li et al., 2016). Here, large-scale MTDs are grouped together to form the Baiyun Submarine Slide Complex (BSSC), and cover an area of more than 10,000 km^2. They are imaged on multibeam bathymetry and 2D/3D seismic data on the continental slope off the Pearl River Mouth Basin (Sun et al., 2008; Li et al., 2014; Wang et al., 2014; Sun et al., 2017). The BSSC is composed of, at least, three vertically stacked MTDs, which were respectively emplaced at 0.19 Ma, 0.50 Ma and 1.59 Ma before present (Sun et al., 2017). Small-scale MTDs were probably caused by local tectonic oversteepening working in association with differences in the rheological behaviour of continental-slope strata (He et al., 2014; Li et al., 2016).

Recently, the origin of the BSSC was proposed to be more complex that previously assumed, as Wang et al. (2014) proposed that the Dongsha Tectonic Event as a key triggering factor of slope instability in the South China Sea. In parallel, Li et al. (2014) suggested that excess pore pressure aided by volcanic activity, tectonic oversteepeing and gas hydrate dissociation, were the major triggering factors for the BSSC. This latter interpretation is possibly correct for parts of the BSSC, but there is no direct evidence to support them in the study area. After a detailed interpretation of new high-resolution 3D seismic data, the distribution of coarse-grained strata (turbidites) and associated seabed topographic highs, were found to be important in controlling the location of MTDs headwall scarps in parts of the South China Sea (Sun et al., 2017).

As the analysis of MTDs in the northern South China Sea is still in its infancy, and the importance of fluid migration in the triggering of MTDs has not been fully addressed, this paper focus on free gas accumulated below individual (Late Cenozoic) MTDs. A significant volume of free gas trapped by MTDs is clearly imaged in two high-quality 3D seismic surveys, providing an unique opportunity to explore their dual relationship. Hence, this work will address the following research questions:

1) What is the relationship between MTDs and underlying free gas in the Pearl River Mouth Basin?
2) What are the main paths for fluid migrating from below the studied MTDs?
3) What processes enhance the seal competence of MTDs in the Pearl River Mouth Basin?
4) What is the importance of the interpreted MTDs, and associated free gas, to future geohazard assessments in the Pearl River Mouth Basin and other continental margins?

2. Geological setting

The South China Sea is the largest and deepest marginal sea in the western Pacific Ocean and kept its present position since the Middle Miocene (Taylor and Hayes, 1983). Five major Cenozoic rift basins were formed along its northern margin, the Qiongdongnan, Pearl River Mouth, Yinggehai, Taixinan Basin, and Beibuwan Basins (Fig. 1). The structural evolution of these sedimentary basins is divided in three stages: a) an Eocene-Early Oligocene rift stage, b) a Neogene-Quaternary post-rift stage characterised by thermal subsidence, and c) a Late Oligocene transitional stage (Ru and Pigott, 1986; Gong and Li, 1997; Zhao et al., 2016) (Fig. 2). Except for regional tectonic movements, which occurred during the Late Miocene and caused local uplift and faulting (Lüdmann and Wong, 1999), tectonic activity was relatively moderate in the Pearl River Mouth Basin during the post-rift stage (Zhou et al., 1995) (Fig. 2).

The two 3D seismic surveys interpreted in this study are located on the continental slope off the Pearl River Mouth Basin (Fig. 1a). The Pearl River Mouth Basin lies in the central part of the northern South China Sea and occupies an area of 17.5×10^4 km^2 (Sun et al., 2012) (Fig. 1). It is the most favourable region for hydrocarbon exploration in the northern margin of the South China Sea (Gong and Li, 1997; Dong et al., 2009). In response to its structural evolution, depositional environments in the Pearl River Mouth Basin changed from lacustrine in its early evolution stages (Eocene-Oligocene rifting), to shallow marine (embayment), and finally open marine during Neogene-Quaternary post-rift (Zhu et al., 2009; Sun et al., 2012) (Fig. 2). Eocene-Lower Oligocene lacustrine strata (mudstone, black shale and coal) have a thickness of more than 2000 m and comprise the main hydrocarbon source interval in the Pearl River Mouth Basin (Zhang and Huang, 1991; Huang et al., 2003). Deltaic depositional systems dominated the margins of the Pearl River Mouth Basin during the Early Miocene and deposited fine-grained strata with a total thickness of 2000–3500 m. These latter strata act as a regional seal for hydrocarbon prospects in the region (Zhu et al., 2009).

3. Data and methods

Two 3D seismic volumes acquired in two distinct regions (Zones A and B) are used in this study (Fig. 1). In Zone A, the interpreted seismic volume covers an area of 2,000 km^2 and was acquired by the China Oilfield Services Limited in 2006. For the acquisition of the seismic volume were used a 3,000 m long streamer containing 240 channels (trace interval 12.5 m), and an array of tuned air guns with a total volume of 8×20 inch^3, working at a shot interval of 25 m. The seismic data in Zone A is zero phased and has a frequency of 45 Hz. The 3D seismic volume has a bin dimension of 12.5×12.5 m and a 2 ms vertical sampling interval. The vertical seismic resolution is 9 m for the depth of MTDs interpreted in this work.

The 3D seismic data in Zone B covers an area of 300 km^2. It was acquired by the China National Offshore Oil Corporation in 2008. The seismic acquisition system consisted of a 3,000 m-long, 120-channel streamer with a hydrophone group interval of 25 m and a sampling interval of 4 ms. The bin spacing of the time-migrated volume is 12.5×12.5 m. The 3D seismic data is zero phased and has a dominant frequency of 35 Hz. The vertical seismic resolution of this 3D seismic survey is 11 m for the depth of MTDs interpreted in this paper.

There are no available borehole data in the study area and, therefore, a p-wave velocity of 1540 m/s was used in our thickness calculations based on data from ODP Site 1146, located 46 km to the east of Zone A (Figs. 1 and 3). The shallow strata drilled at ODP Site 1146 is dominated by fine-grained nannofossil clay (Fig. 3).

Seismic interpretation consisted in the mapping of the top and base of MTDs, computing and extracting variance volumes and slices, calculating RMS (root-mean square) amplitude maps, and computing isochron data on Schlumberger's Geoframe® 2012. After mapping the top

and base of different MTDs, their areas and volumes were also calculated on Geoframe® 2012.

In order to understand the petrophysical character of the MTDs in this study we compared ODP borehole data from the South China Sea with IODP and ODP data from the Gulf of Mexico and Amazon Fan, located in similar depositional environments to the study area, and presenting similar lithologies. Borehole data (including wireline logs) were obtained from the IODP/ODP database (http://brg.ldeo.columbia.edu/logdb/files.php and http://www-odp.tamu.edu/publications/pubs_pr.htm) and provided by D.J.W. Piper (pers. comm.). The original log data was downloaded on Carbon 3.0. Sediment porosity (ø) in Site U1323 was calculated using the following equation:

$$ø = (\rho_b - \rho_g)/(\rho_w - \rho_g) \quad (1)$$

where ρ_g and ρ_w are pore fluid density and solid-grain density, respectively (Dugan, 2012).

4. Evidence of gas trapping at the base of MTDs in the Pearl River Mouth Basin

Enhanced negative seismic anomalies (ENSAs) are observed along the base of chaotic MTDs in Zone A (Figs. 4a-e). They occur around the MTDs' headwall scarps, but often continue into undisturbed strata to the east (i.e. upslope) of these same headwall regions (Figs. 4a-b, 4e). The ENSAs are discrete circular features, or present a linear distribution; they abruptly contact with non-enhanced seismic reflections (Fig. 4). To the west, they contact with high-amplitude strata with a thickness reaching 230 m, and onlapping seismic reflections being also observed (Fig. 4b). To the north and east, the interpreted ENSAs are bounded by low-amplitude features (Fig. 4e). However, their western limit is difficult to identify because of the predominance of high-amplitude strata in this same area. Thus, the black continuous line in Fig. 4b is the conservative limit of ENSAs to the west, providing a conservative area of ~18 km^2, and a volume approaching 0.44 km^3 (Fig. 4e and Table 1).

In Zone B, acoustic anomalies observed on seismic and RMS-amplitude data are vertically stacked (Figs. 5 and 6). These stacked enhanced seismic anomalies (SESAs) are trapped underneath chaotic MTDs (Figs. 5a and 5b) and are sub-circular in plan view (Fig. 7). They occur along, or instead cross-cut, slope strata and seismic reflections that show a lateral inversion in polarity in these features (Figs. 6c-d). Several chaotic and dimmed seismic reflections sourced from deeper strata are observed directly below the SESAs (Figs. 5a-b, 6a). Their thickness is variable and shows four maxima that correlate with the underlying chaotic and dimmed seismic reflections (Figs. 5 to 7). The SESAs cover an area of 30.58 km^2 (Fig. 5c; Table 1), and abruptly terminate to the west where they are bounded by a large normal fault (Figs. 5a-b).

Negative seismic anomalies observed at the base of MTDs are usually interpreted as basal shear zones, and are generated by differences in acoustic impedance between MTDs and underlying strata (Dugan, 2012). Therefore, the ENSAs observed in Zone A occur in basal shear zones as documented in Alves and Lourenço (2010) and Dugan (2012). Yet, they extend laterally beyond the MTDs (Figs. 4a-d), a character suggesting they are not basal shear zones through their whole extent. A sharp boundary at the gas hydrate stability zone (i.e., a bottom-simulating reflection or BSR) is another possible explanation for the origin of these negative acoustic anomalies. However, the ENSAs are not parallel to the seabed (Figs. 4a-d), indicating that they are not BSRs. Their abrupt contact with the surrounding strata is similar to the seismic character of free gas documented in multiple studies (e.g. Cartwright et al., 2007; Judd and Hovland, 2007; Sun et al., 2012) and, thus, the ENSAs observed in Zone A are interpreted as free gas. In contrast, the parallel high-amplitude seismic reflections in the western part of Fig. 4b and Fig. 4e are sub-parallel, and probably caused by strata with different physical properties to the imaged MTDs. They are interpreted as coarse-grained turbidites (Sun et al., 2017) i.e., likely regions with a high sand content as those documented by Gamboa et a. (2010) in SE Brazil.

The internal seismic character of SESAs in Zone B is distinct from that in ENSAs (free gas) and parallel high-amplitude seismic reflections (turbidites) in Zone A (Figs. 5 and 6). The SESAs are vertically stacked and show an inversion in seismic polarity, at places cross-cutting the slope strata (Figs. 6c-d). This character is typical of free gas accumulations (e.g. Judd and Hovland, 2007; Brown, 2011; Sun et al., 2012), and the SESAs in Zone B are also interpreted as comprising free gas in the

interior of porous sediment. The chaotic and dimmed seismic reflections directly below the free gas zone are interpreted as pathways (gas chimneys) for the migration of free gas (Figs. 5 to 7).

5. Seismic characteristics of gas-laden MTDs

5.1 Mass-transport deposits in Zone A

Shallow strata in Zone A are characterised by the interbedding of chaotic to parallel seismic reflections (Fig. 8). The chaotic seismic reflections in Zone A are similar to the seismic character of MTDs documented on many passive and active continental margins (e.g. Evans et al., 1996; Bøe et al., 2000; Imbo et al., 2003; Frey Martinez et al., 2005; Gee et al., 2006; Moscardelli et al., 2006; Bull et al., 2009; Omosanya and Alves, 2013; Gong et al., 2014; Li et al., 2014; Wang et al., 2014). Therefore, chaotic seismic reflections are interpreted as MTDs, here informally named MTDa. This MTDa extends beyond the coverage of 3D seismic data, with only its eastern part being well imaged (Fig. 4).

Apart from their chaotic seismic reflections, short sub-parallel seismic reflections are also observed within MTDa (Figs. 8b-c). They occur as structures accumulated close to headwall scarps or, in other regions of MTDa, as pointy features observed on seismic and coherence data (Fig. 9). Similarly to structures reported in Bull et al. (2009) and Alves. (2015), the pointy features are interpreted as linear blocks accumulated in the extensional domain of MTDa. The features are interpreted as rafted blocks that can occur at any zone within MTDs (Alves, 2015); 'ridge-like' structures are often observed and usually rise over, or pierce, the overlying strata (Figs. 8b-c). At places, onlapping seismic reflections occur at the flanks of these same ridges, indicating that the deposition of these onlapping strata occurred during, or immediately after, the emplacement of MTDa (Figs. 8b and 8d).

A steep headwall scarp is observed on seismic data, and has an elevation ranging from 60 to 95 m (Fig. 8). It is arcuate in plan view and extends from NW to SE (Fig. 9). At this same scarp, MTDa contacts with undeformed slope deposits that are observed to the east (Figs. 8c-d). In addition, a thin unit with near-constant thickness (~65.0 m) drapes and overlies MTDa.

MTDa has variable thickness, with an average value of 55.3 m (Table 1). The maximum thickness of MTDs is ~100 m and occurs against the headwall scarp (Fig. 8a). In detail, MTDa becomes thinner downslope from its headwall scarp, towards to west (Fig. 8a). MTDa extends beyond the 3D seismic survey to the west and south and cover an area of 69.5 km^2 (Table 1). Thus, 3.84 km^3 of remobilized strata are accumulated in Zone A. As both Zone A and the area around ODP Site 1146 are located in deep waters and far from the modern shelf break of the northern South China Sea, MTDa is likely composed of fine-grained deposits similar to those drilled at ODP Site 1146 (Fig. 3).

5.2 Mass-transport deposits in Zone B

Shallow strata in Zone B are wedge-shaped, with strata onlapping both the western and northern parts of the study area (Figs. 5a-b, 6a-b). Six seismic anomalies (informally named MTDb1 - MTDb6) are identified in Zone B. They have similar seismic characters to strata in MTDa and are interpreted to comprise MTDs (Figs. 5a-b, 6a-b). Locally, parallel seismic reflections are observed within these deposits, while sharp pointy features observed on coherent data and are interpreted as rafted blocks (Fig. 10). The uppermost two MTDs (MTDb1 and MTDb2) extend regionally to continue beyond Zone B (Figs. 10a, 11). The intermediate MTDs (MTDb3 and MTDb4) have smaller sizes and limited distributions compared to the other four MTDs. The lowermost MTDs (MTDb5 and MTDb6) are bounded to the west and north by, and onlap, continental-slope strata (Figs. 5a-b, 6a-b).

MTDb1 covers an area of 63.4 km^2 and has an average thickness of 27.2 m (Fig. 11; Table 1). Two thickness maxima are observed in the northeastern and central-western parts of MTDb1 (Fig. 11). Grooves caused by the scouring of rafted (remobilised) blocks, and often parallel to the flow directions of rafted blocks (Posamentier and Kolla, 2003; Moscardelli et al., 2006; Sun et al., 2011), are clearly identified at the base of MTDb1 (Fig. 10a). They strike roughly to the NW, indicating that strata were transported to the SE. Towards to the southern part of Zone B (downslope), MTDb1 becomes thinner and pinches out. MTDb2 has a similar distribution to MTDb1 and NW-SE grooves are also observed (Fig. 10b). However, MTDb3 and MTDb4 are limited to the central-northern part of the 3D seismic

survey (Fig. 12). In comparison, MTDb5 and MTDb6 have a similar distribution and cover areas of 51.4 km^2 and 46.9 km^2, respectively (Fig. 12; Table 1). Rafted blocks and NW-trending grooves are also observed at the base of MTDb6 (Fig. 10c), indicating that all six (6) MTDs were sourced from the upper slope and moved towards the SE. MTDb5 and MTDb6 have a total thickness of ~55.8 m, and overlay the main body of free gas at depth (Fig. 11).

6. Discussion

6.1 Seal capacity of mass-transport deposits

The relationship between free gas and MTDs has been previously assessed in the literature, with free gas being usually proposed as an important trigger of MTDs (e.g. Bünz et al., 2005; Wang et al., 2014). However, the two examples in this study show that free gas is directly trapped underneath MTDs, and that these deposits form competent seal intervals to promote lateral migration of gas into undeformed slope strata. There are no wells drilled through the MTDs investigated in this paper and, thus, the petrophysical properties of MTDs cannot be directly assessed. Yet, the MTDs in the study area are likely fine-grained as deduced from units drilled at ODP Site 1146, and are similar to strata documented in the Amazon Fan (Piper et al., 1997; Shipp et al., 2004), Nankai Accretionary Wedge (Strasser et al., 2011), Gulf of Mexico (Dugan, 2012), Ulleung Basin (Riedel et al., 2012) and Arabian Sea (Pandey et al., 2015). The MTDs in these locations were drilled by ODP/IODP and exploration wells. Moreover, all MTDs documented in the these regions showed similar petrophysical characteristics (e.g. Piper et al., 1997; Dugan, 2012; Riedel et al., 2012; Alves et al., 2014; Pandey et al., 2015), suggesting that the petrophysical character of these same deposits is predictable and probably associated with a common lithology. Hence, the petrophysical data acquired by previous ODP/IODP expeditions can be used in this study.

The shear deformation caused by the mass movement changes the petrophysical character of slope strata (Shipp et al., 2004; Dugan, 2012). The bulk density and porosity of MTDs in the Gulf of Mexico is ~7% higher and ~14% lower than the underlying and overlying undeformed strata, respectively (Fig. 13a). The denser (and lower porosity) strata in MTDs will cause the compressional wave and resistivity to be higher than confining, non-disturbed sediment (Fig. 13b), with shear deformation also contributing to the loss of water in MTDs (Piper et al., 1997; Shipp et al., 2004). For instance, the water content of MTDs in the Amazon Fan is ~30% lower than normal strata (Fig. 13b). Therefore, the MTDs are more consolidated than the overlying and underlying normally depositional strata and have a larger capacity to serve as seals than undeformed strata, because of the higher bulk density, lower porosity and water content of MTDs. This could justify why the free gas is trapped underneath the MTDs observed in the study area.

In Zone A, vertical migration pathways below free gas (e.g. tectonic faults, gas chimneys and mud diapirs) are not observed and free gas is laterally connected to continuous high-amplitude strata (Figs. 4b and 4e). These strata are interpreted as coarse-grained turbidites similar to those reported in the Espírito Santo Basin (Gamboa et al., 2010). Thus, the free gas is probably sourced from deeper strata below the MTDs and migrates upwards along these porous strata (Fig. 14a). When the free gas reaches the MTDs is sealed and cannot vertically migrate, but can laterally migrate updip along the base of MTDs (basal shear zone) or along the porous strata just below these latter. This phenomenon generates the ENSAs observed beyond the scarp of MTDs in Zone A (Figs. 4b, 14a).

Free gas is also sourced from deeper strata in Zone B. However, it migrates upwards along gas chimneys or faults as observed in Figs. 5-6 and 14b. In parallel, the distribution of free gas in Zone B is mainly controlled by their migration pathways and accumulated at the top of gas chimneys and faults as observed in Fig. 7. The gas chimneys are likely composed of fractures and small faults, and provide efficient pathways for fluid migration (Cathes et al., 2010). The transported fluids (gas) are obstructed by the more consolidated MTDs in Zone B and trapped within porous strata below the MTDs (Figs. 14b).

6.2 Mass-transport deposits and their importance as offshore geohazards in the South China Sea

Mass-transport deposits are considered to be significant geohazards when triggered on continental slopes (e.g. Moscardelli et al., 2006; Migeon et al., 2011). The large volumes and long transporting distances of strata involved in their *en-masse* transport have enough power to destroy

offshore infrastructures or, at times, trigger large destructive tsunamis with the potential of sweeping through low-lying coastal zones. For example, the tsunami triggered by the Storegga slide impacted the coasts of the Norwegian Sea, northern North Sea and southeastern North Sea (e.g. Long et al., 1989; Smith et al., 2004; Bondevik et al., 2005; Friergaard et al., 2015). However, the importance of MTDs as geohazards after their emplacement is seldom assessed. This study considers two main implications of MTDs and trapped free gas for future geohazard assessments.

First, local overpressure induced by the free gas is a significant hazard during drilling, particularly when considering the large volumes of free gas identified underneath the two MTDs in this study. Considering that the two MTDs are more consolidated than undeformed slope strata, overpressure will build underneath them. The free gas and consequent overpressure will greatly affect borehole stability during drilling in such an hydrocarbon-rich basin as the Pearl River Mouth Basin.

Second, the free gas-charged strata possibly serve as weak layers for new slope failures. In this study, trapped free gas under over-consolidated MTDs migrates laterally along the basal shear zone, and likely through porous strata located just underneath the MTDs. This free gas later migrates into the undeformed strata beyond the scarps of MTDs (e.g. Zone A; Figs. 4a-d). Here, the gas-bearing strata could possibly serve as weak layers and the strata overlying them will fail under certain conditions, such as during regional earthquakes. Therefore, new slope failures will occur and will share the same basal surface with the previous MTDs. This process probably contributed to the retrogressive failure of MTDs in the South China Sea, and other continental margins.

7. Conclusions

Mass-transport deposits and free gas were documented using two high-quality 3D seismic volumes. The main conclusions of this work can be summarised as follows:

a) The MTDs are characterised by chaotic reflections, scarps and low coherence. In turn, free gas is revealed in the form of enhanced (bright) negative seismic reflections, or by stacked features of reversed polarity and cross-cutting strata;

b) The free gas is directly trapped under the interpreted MTDs, which suggests they act as competent seals to hinder the vertical migration of free gas. However, the trapped free gas migrates updip beyond the scarps (and basal shear zones) of MTDs;

c) The trapped free gas migrates vertically from deeper sources via gas chimneys, faults and porous strata.

d) The seal competence of MTDs depends on petrophysical properties such as density, water content and porosity. These properties drive the MTDs to achieve a more consolidated state than adjacent (undeformed) slope strata;

e) Overpressure caused by trapped free gas under the MTDs is a likely geohazard that must be taken into account when drilling through MTDs;

f) The lateral migration of free gas is likely to generate new mass wasting on continental slopes. It potentially triggers multi-stage slope failure and can be responsible for the retrogressive evolution of MTDs on continental margins.

Acknowledgements

This work was supported by the National Scientific Foundation of China (Grant Nos. 41306054, 41372112 and 91228202), the National Basic Research Program of China (2015CB251201) and the Programme of Introducing Talents of Discipline to Universities (No. B14031). We thank China National Offshore Oil Company for permission to release the data. We are grateful to an anonymous reviewer, Dr. Chenglin Gong and Associate Editor Alejandro Escalona for their helpful comments and suggestions which greatly improved our manuscript.

References

Alves, T.M., 2010. 3D Seismic examples of differential compaction in mass-transport deposits and their effect on post-failure strata. Marine Geology, 271: 212–224.

Alves, T.M., 2015. Submarine slide blocks and associated soft-sediment deformation in deep-water basins: A review. Marine and Petroleum Geology, 67: 262-285.

Alves, T.M., Cartwright, J.A., 2009. Volume balance of a submarine landslide in the Espírito Santo Basin, offshore Brazil: quantifying seafloor erosion, sediment accumulation and depletion. Earth and Planetary

Science Letters, 288: 572-580.

Alves, T.M., Kurtev, K., Moore, G.F., Strasser, M., 2014. Assessing the internal character, reservoir potential and seal competence of mass-transport deposits using seismic texture: a geophysical and petrophysical approach. AAPG Bulletin, 98: 911-945.

Alves, T.M., Lourenco, S., 2010. Geomorphologic features related to gravitational collapse: submarine landsliding to lateral spreading on a Late Miocene-Quaternary slope (SE Crete, eastern Mediterranean). Geomorphology, 123: 13-33.

Best, A., Clayton, C., Longva, O., Szuman, M., 2003. The role of free gas in the activation of submarine slides in Finneidfjord. In: Locat J, Mienert J, Boisvert L (eds) Submarine Mass Movements and Their Consequences, 1st Int Symp. Advances in Natural and Technological Hazards Research, vol 19. Springer, Dordrecht, pp 491–498.

Bøe, R., Hovland, M., Instanes, A., Rise, L., Vasshus, S., 2000. Submarine slide scars and mass movements in Karmsundetand Skudenedfjorden, southwestern Norway: morphology and evolution. Marine Geology, 167: 147–165.

Bondevik, S., Mangerud, J., Dawson, S., Dawson, A., Lohne, Ø., 2005. Evidence for three North Sea tsunamis at the Shetland Islands between 8000 and 1500 years ago. Quaternary Science Reviews, 24: 1757-1775.

Brown, A.R., 2011. Interpretion of three-dimensional seismic data (seventh edition). AAPG Memoir 42 (Tulsa, OK).

Bull, S., Cartwright, J.. Huuse, M., 2009. A review of kinematic indicators from mass-transport complexes using 3D seismic data. Marine and Petroleum Geology, 26: 1132–1151.

Bünz, S., Mienert, J., Bryn, P., Berg, K., 2005. Fluid flow impact on slope failure from 3D seismic data: A case study in the Storegga Slide. Basin Research, 17: 109–122.

Cartwright, J.A., Huuse, M., Aplin, A., 2007. Seal bypass systems. AAPG Bulletin, 91: 1141–1166.

Cathles, L.M., Su, Z., Chen, D.F., 2010. The physics of gas chimney and pockmark formation, with implications for assessment of seafloor hazards and gas sequestration. Marine and Petroleum Geology, 27: 82-91.

Chadwick, W., Dziak, R., Haxel, J., Embley, R., Matsumoto, H., 2012. Submarine landslide triggered by volcanic eruption recorded by in situ hydrophone. Geology, 40:51–54.

Dalla Valle, G., Gamberi, F., Rocchini, P., Minisini, D., Errera, A., Baglioni, L., Trincardi, F., 2013. 3D seismic geomorphology of mass transport complexes in a foredeep basin: examples from the Pleistocene of the CentralAdriatic Basin (Mediterranean Sea). Sedimentary Geology, 294: 127–141.

Dickinson, J.A., Ware, K., Cosham, S., Murphy, B., 2012. Slope failure and canyon development along the northern South China Sea marin, in Y. Yamada et al. (eds.), Submarine Mass Movements and Their Consequences, 31: 223-232.

Dong, D., Zhang, G., Zhong, K., Yuan, S. & Wu, S. 2009. Tectonic evolution and dynamics of deepwater area of Pearl River Mouth Leynaud, D., Sultan, N. & Mienert, J. 2007. The basin, northern South China Sea. Journal of Earth Science, 20: 147–159.

Dugan, B., 2012. Petrophysical and consolidation behavior of mass transport deposits from the northern Gulf of Mexico, IODP Expedition. Marine Geology, 315-318: 98-107.

Dugan, B., Flemings, P.B., 2000. Overpressure and fluid flow in the New Jersey continental slope: implications for slope failure and cold seeps. Science, 289: 288–291.

Evans, D., King, E.L., Kenyon, N.H., Brett, C., Wallis, D., 1996. Evidence for long-term instability in the Storegga Slide region off western Norway. Marine Geology, 130: 281–292.

Frey Martinez, J., Cartwright, J., Hall, B., 2005. 3D seismic interpretation of slump complexes: examples from the continental margin of Israel. Basin Research, 17: 83–108.

Fruergaard, M., Piasecki, S., Johannessen, P.N., Noe-Nygaard, N., Andersen, T.J., Pejrup, M., Nielsen, L.H., 2015. Tsunami propagation over a wide, shallow continental shelf caused by the Storegga slide, southeastern North Sea, Denmark. Geology, 43: 1047-1050.

Gamboa, D., Alves, T., Cartwright, J., Terrinha, P., 2010. MTD distribution on a 'passive' continental margin: The Espírito Santo Basin (SE Brazil) during the Palaeogene. Marine and Petroleum Geology, 27: 1311-1324.

Gee, M.J.R., Gawthorpe, R.L., Friedmann, S.J., 2006. Triggering and evolution of a giant landslide, offshore Angola revealed by 3D seismic stratigraphy and geomorphology. Journal of Sedimentary Research, 76: 9–19.

Gong, C.L., Wang, Y.M., Hodgson, D.M., Zhu, W.L., Li, W.G., Xu, Q., Li, D., 2014. Origin and anatomy of two different types of mass transport complexes: A 3D seismic case study from the northern South China Sea margin. Marine and Petroleum Geology, 54: 198-215.

Gong, C.L., Wang, Y.M., Zhu, W.L., Li, W.G., Xu, Q., 2013. Upper Miocene to Quaternary unidirectionally migrating deep-water channels in the Pearl River Mouth Basin, northern South China Sea. AAPG Bulletin, 97: 285-308.

Gong, Z.S., Li, S.T. 1997. Continental Margin Basin Analysis and Hydrocarbon Accumulation of the Northern South China Sea. Science Press, Beijing, 193–256.

Haflidason, H., Sejrup, H.P., Nygård, A., Mienert, J., Bryn, P., Lien, R., Forsberg, C.F., Berg, K., Masson, D., 2004. The Storegga Slide: architecture, geometry and slide development. Marine Geology, 213: 201–234.

Hampton, M.A., Lee, H.J., Locat, J., 1996. Submarine landslides. Review of Geophysics, 34: 33–59.

Hance, J.J., 2003. Development of a database and assessment of seafloor slope stability based on published literature. MS thesis, University of

Texas at Austin.

He, Y., Zhong, G.F., Wang, L.L., Kuang, Z.G., 2014. Characteristics and occurrence of submarine canyon-associated landslides in the middle of the northern continental slope, South China Sea. Marine and Petroleum Geology, 57: 546-560.

Huang, B.J., Xiao, X.M., Zhang, M.Q., 2003. Geochemistry, grouping and origins of crude oils in the Western Pearl River Mouth Basin, offshore South China Sea. Organic Geochemistry, 34: 993–1008.

Ikari, M.J., Strasser, M., Saffer, D.M., Kopf, A.J., 2011. Submarine landslide potential near the megasplay fault at the Nankai subduction zone. Earth Planetary Science Letters, 312: 453–462.

Imbo, Y., De Batist, M., Canals, M., Prieto, M.J., Baraza, J., 2003. The Gebra Slide: a submarine slide on the Trinity Peninsula Margin, Antarctica. Marine Geology, 193: 235–252.

Judd, A.G., Hovland, M., 2007. Seabed Fluid Flow: The Impact on Geology, Biology and the Marine Environment. Cambridge University Press, Cambridge, pp. 163–178.

Krastel, S., Wynn, R.B., Hanebuth, T.J.J., Henrich, R., Holz, C., Meggers, H., Kuhlmann, H., Georgiopoulou, A., Schulz, H.D., 2006. Mapping of seabed morphology and shallow sediment structure of the Mauritania continental margin, Northwest Africa: some implications for geohazard potential. Norsk Geologisk Tidsskrift, 86: 163-176.

Laberg, J.S., Kawamura, K., Amundsen, H., Baeten, N., Forwick, M., Rydningen, T.A., Vorren, T.O., 2014. A submarine landslide complex affecting the Jan Mayen Ridge, Norwegian–Greenland Sea: slidescar morphology and processes of sediment evacuation. Geo-Mar Letters, 34: 51–58.

Laberg, J.S., Vorren, T.O., 2000. The Trænadjupet Slide, offshore Norway-morphology, evacuation and triggering mechanisms. Marine Geology, 171: 95–114.

Lastras, G., Canals, M., Hughes-Clarke, J.E., Moreno, A., De Batist, M., Masson, D.G., Cochonat, P., 2002. Seafloor imagery from the BIG'95 debris flow, western Mediterranean. Geology 30, 871–874.

Li, W., Alves, T.M., Wu, S.G., Rebesco, M., Zhao, F., Mi, L.J., 2016. A giant, submarine creep zone as a precursor of large-scale slope instability offshore the Dongsha Islands (South China Sea). Earth and Planetary Science Letters, 451: 272-284.

Li, W., Wu, S.G., Völker, D., Zhao, F., Mi, L.J., Kopf, A., 2014. Morphology, seismic characterization and sediment dynamics of the Baiyun Slide Complex on the northern South China Sea margin. Journal of the Geological Society, London, 171: 865-877.

Li, X.S., Zhou, Q.J., Su, T.Y., Liu, L.J., Gao, S., Zhou, S.W., 2016. Slope-confined submarine canyons in the Baiyun deep-water area, northern South China Sea: variation in their modern morphology. Marine Geophysical Research, 37: 95-112.

Lo Iacono, C., Gràcia, E., Zaniboni, F., Pagnoni, G., Tinti, S., Bartolomé, R., Masson, D.G., Wynn, R.B., Lourenço, N., Pinto de Abreu, M., Dañobeitia, J.J., Zitellini, N., 2012. Large, deepwater slope failures: implications for landslide-generated tsunamis. Geology, 40: 931–934.

Locat, J., Lee, H.J., 2002. Submarine landslides: advances and challenges. Canadian Geotechnical Journal, 39: 193-212.

Long, D., Smith, D.E., Dawson, A.G., 1989. A Holocene tsunami deposit in eastern Scotland. Journal of Quaternary Science, 4: 61-66.

Lüdmann, T., Wong, H.K., 1999. Neotectonic regime on the passive continental margin of the northern South China Sea. Tectonophysics, 311: 113–138.

Martinsen, O.J., 1994. Mass movements. In: Maltman, A. (Ed.), The Geological Deformation of Sediments. Chapman & Hall, London, pp. 127–165.

Maslin, M., Vilela, C., Mikkelsen, N., Grootes, P., 2005. Causes of catastrophic sediment failures of the Amazon Fan. Quaternary Science Review, 24: 2180–2193.

Masson, D.G., Harbitz, C.B., Wynn, R.B., Pedersen, G., Lovholt, F., 2006. Submarine landslides: processes, triggers and hazard prediction. Philosophical Transactions. Series A, Mathematical, Physical, and Engineering Sciences, 364: 2009-2039.

Migeon, S., Cattaneo, A., Hassoun, V., Larroque, C., Corradi, N., Fanucci, F., Dano, A., de Lepinay, B.M., Sage, F., Gorini, C., 2011. Morphology, distribution and origin of recent submarine landslides of Ligurian Margin (North-western Mediterranean): some insights into geohazard assessment. Marine Geophysical Research, 32: 225-243.

Moscardelli, L., Wood, L., Mann, P., 2006. Mass-transport complexes and associated processes in the offshore area of Trinidad and Venezuela. AAPG Bulletin, 90: 1059–1088.

Noda, A., TuZino, T., Joshima, M., Goto, S., 2013. Mass transport-dominated sedimentation in a foreland basin, the Hidaka Trough, northern Japan. Geochemistry Geophysics Geosystems, 14:2638–2660.

Omosanya, K. O., Alves, T. M., 2013. Ramps and flats of mass-transport deposits (MTDs) as markers of seafloor strain on the flanks of rising diapirs (Espírito Santo Basin, SE Brazil). Marine Geology ,340: 82-97.

Pandey, D.K., Clift, P.D., Kulhanek, D.K., Andò, S., Bendle, J.A.P., Bratenkov, S., Griffith, E.M., Gurumurthy, G.P., Hahn, A., Iwai, M., Khim, B.-K., Kumar, A., Kumar, A.G., Liddy, H.M., Lu., H., Lyle, M.W., Mishra, R., Radhakrishna, T., Routledge, C.M., Saraswat, R., Saxena, R., Scardia, G., Sharma, G.K., Singh, A.D., Steinke, S., Suzuki, K., Tauxe, L., Tiwari, M., Xu, Z., Yu, Z., 2015. Expedition 355 Preliminary Report: Arabian Sea Monsoon. International Ocean Discovery Program. http://dx.doi.org/10.14379/iodp.pr.355.2015

Pang, X., Chen, C.M., Peng, D.J., Zhou, D., Shao, L., He, M., Liu, B.J., 2008. Basic geology of Baiyun deep-water area in the northern South China Sea. China Offshore Oil and Gas, 20: 216-222.

Prior, D.B., Bornhold, B.D., Johns, M.W., 1984. Depositional characteristics

of a submarine debris flow. Journal of Geology 92, 707–727.

Posamentier, H.W., Kolla, V., 2003. Seismic geomorphology and stratigraphy of depositional elements in deep-water settings. Journal of Sedimentary Research, 73:367–388.

Riedel, M., Bahk, J.J., Scholz, N.A., Ryu, B.J., Yoo, D.G., Kim, W., Kim, G.Y., 2012. Mass-transport deposits and gas hydrate occurrences in the Ulleung Basin, East Sea e Part 2: Gas hydrate content and fracture-induced anisotropy. Marine and Petroleum Geology, 35: 75-90.

Ru, K., Pigott, J.D., 1986. Episodic rifting and subsidence in the South China Sea. AAPG Bulletin, 70:1136–1155.

Shipp, R.C., Nott, J.A., Newlin, J.A., 2004. Physical characteristics and impact of mass transport complexes on deepwater jetted conductors and suction anchor piles. In: Offshore Technology Conference, Houston, Texas.

Smith, D.E., Shi, S., Cullingford, R.A., Dawson, Alastair G., Dawson, S., Firth, C.R., Foster, Ian D.L., Fretwell, P.T., Haggart, B.A., Holloway, L.K., Long, D., 2004. The Holocene Storegga Slide tsunami in the United Kingdom. Quaternary Science Reviews, 23: 2291-2321.

Soares, D.M., Alves, T.M., Terrinha, P., 2012. The breakup sequence and associated lithospheric breakup surface: their significance in the context of rifted continental margins (West Iberia and Newfoundland margins, North Atlantic). Earth and Planetary Science Letters, 355-56: 311-326.

Strasser, M., Moore, G.F., Kimura, G., Kopf, A.J., Underwood, M.B., Guo, J.H., Screaton, E.J., 2011. Slumping and mass transport deposition in the Nankai fore arc: Evidence from IODP drilling and 3-D reflection seismic data. Geochemistry, Geophysics, Geosystems,12: Q0AD13.

Strozyk, F., Strasser, M., Förster, A., Kopf, A., Huhn, K., 2010. Slope failure repetition in active margin environments: constraints from submarine landslides in the Hellenic fore arc, eastern Mediterranean. Journal of Geophysical Research, 115: B08103.

Sun, Q.L., Wu, S.G., Cartwright, J., Wang, S.H., Lu, Y.T., Chen, D.X., Dong, D.D., 2014. Neogene igneous intrusions in the northern South China Sea: Evidence from high-resolution three dimensional seismic data. Marine and Petroleum Geology, 54:83-95.

Sun, Q.L., Wu, S.G., Cartwright, J.A., Dong, D.D., 2012. Shallow gas and focused fluid flow systems in the Pearl River Mouth Basin, northern South China Sea. Marine Geology, 315-318: 1-14.

Sun, Q.L., Xie, X.N., Piper, D.J.W., Wu, J., Wu, S.G., 2017. Three dimensional seismic anatomy of multi-stage mass transport deposits in the Pearl River Mouth Basin, northern South China Sea: Their ages, kinematics and controlling factors. Marine Geology, in press.

Sun, Q.L., Wu, S.G., Lüdmann, T., Wang, B., Yang, T.T., 2011. Geophysical evidence for cyclic sediment deposition on the southern slope of Qiongdongnan Basin, South China Sea. Marine Geophysical Research, 32: 415-428.

Sun, Y.B., Wu, S.G., Wang, Z.J., Li, Q.P., Wang, X.J., Dong, D.D., Liu, F., 2008. The geometry and deformation characteristics of Baiyun Submarine Landslide. Marine Geology & Quaternary Geology, 28: 70-77.

Taylor, B., Hayes, D.E., 1983. Origin and history of the South China Sea basin. In: The Tectonic and Geologic Evolution of Southeast Asian Seas and Islands: Part 2. AGU Geophys Monogr Ser 27:23–56

Varnes, D.J., 1978. Slope movement types and processes. In: Schuster, R.L., Krizek, R.J. (Eds.), Landslides, Analysis and Control. Transportation Research Board Special Report 176. National Academy of Sciences, Washington, pp. 11–33.

Wang, L., Wu, S.G., Li, Q.P., Wang, D.W., Fu, S.Y., 2014. Architecture and development of a multi-stage Baiyun submarine slide complex in the Pearl River Mouth Canyon, northern South China Sea. Geo-marine letter, 34: 327-343.

Wang, P.X., Prell, W., Blum, P., et al., 2000. Initial Reports, 184. In: Proceedings of Ocean Drilling Program. ODP, Texas A&M, College Station, USA.

Zhao, F., Alves, T.M., Wu,S.G., Li,W., Huuse, M., Mi, L.J., Sun, Q.L., Ma, B.J., 2016. Prolonged post-rift magmatism on highly extended crust of divergent continental margins (Baiyun Sag, South China Sea). Earth and Planetary Science Letters, 445: 79-91.

Zhang, Q.X., Huang, B.J., 1991. Genetic types and generation history of natural gases from major basins in the South China Sea. China Offshore Oil & Gas, 4: 5–13.

Zhou, D., Ru, K., Chen, H.Z., 1995. Kinematics of Cenozoic extension on the South China Sea continental margin and its implications for the tectonic evolution of the region. Tectonophysics, 251: 161–177.

Zhu, W., Huang, B., Mi, L., Wilkins, R.W., Fu, N., Xiao, X., 2009. Geochemistry, origin, and deep-water exploration potential of natural gases in the Pearl River Mouth and Qiongdongnan basins, South China Sea. AAPG Bulletin, 93: 741–761.

Figure Captions

Figure 1: (a) Geological setting and location of sedimentary basins in the northern South China Sea. Inset (top left): regional setting. The two study areas (highlighted by the red squares) are located within the Pearl River Mouth Basin (modified from Sun et al., 2012). ODP sites 1144–1148 are labeled; (b) Seabed morphology of Zone A. The MTD scarp is identified; (c) Seabed morphology of Zone B. Pockmarks (P) are observed and numbered.

Figure 2: Schematic stratigraphic column of the Pearl River Mouth Basin (modified from Pang et al. (2008) and Sun et al.

(2014)). The short red lines in 'Tectonic Events' represent the main stages of each tectonic episode.

Figure 3: Composite section of 2D and 3D seismic data crossing ODP Site 1146. MTDa is marked by the light purple polygon. The dashed green and cyan lines highlight the top and base of MTDa. The lines continue into correlative (and undeformed) continental slope strata. Lithology data is from Wang et al. (2000). Well log data is from Sun et al. (2017). DT = acoustic logging; RHOB = density logging. See location in Fig. 1a.

Figure 4: (a)-(d) 3D seismic profiles in Zone A showing the internal character of enhanced negative seismic anomalies (ENSAs) interpreted as free gas in the study area. The ENSAs are trapped underneath MTDa and continue laterally beyond its scarp. The parallel high-amplitude seismic reflections in (b) are interpreted as turbidites. The blue dashed lines in (b) highlight speculative fluid migration pathways (porous strata). The locations of (a)-(d) are labeled in (e); (e) RMS-amplitude map (50 ms (twt) window above and below the basal surface of MTDa) shows the distribution of ENSAs (black dashed line). The boundary (scarps) of MTDa superimposed on this map is shown by the dashed red line. Parallel seismic reflections show higher (RMS) amplitude than free gas.

Figure 5: (a) 3D seismic profile imaging free gas and MTDs in Zone B. (b) Corresponding interpretation of the seismic profile in (a). Six MTDs (MTDb1-MTDb6) showing chaotic seismic reflections and free gas form vertically stacked enhanced seismic anomalies (SESAs) underneath the MTDs. The labelled gas chimneys (blue arrows) and faults (dashed red lines) serve as major fluid pathways. See location of seismic section in (c); (c) RMS-amplitude map of Zone B (80 ms (twt) window below the basal surface of lowermost MTD) highlighting the sub-circular distribution of free gas.

Figure 6: (a) 3D seismic profile highlighting the relationship between free gas and MTDs in Zone B. (b) Corresponding interpretation of the seismic profile in (a). Gas chimneys (marked with blue arrows) are shown as vertical chaotic seismic reflections. Faults (marked with dashed red lines) are also identified. The stacked enhanced seismic anomalies (SESAs) with reversed seismic polarity (c) and cross-cutting seismic reflections (d) are interpreted as free gas.

Figure 7: Isochron thickness map of gas-bearing strata (stacked enhanced seismic anomalies) in Zone B. Several depocenters are identified and correlate with fluid migration pathways (gas chimneys and faults).

Figure 8: (a) Isochron thickness map for MTDa, Zone A. The thickness of MTDa is variable and is reduced from the scarp (northeast) downslope (southwest). (b)-(c) Internal seismic character (chaotic seismic reflections) of MTDa in Zone A. The dashed blue lines are speculative fluid migration pathways (porous strata) interpreted in the study area. ENSAs (enhanced negative-phased seismic anomalies, free gas), blocks, internal ridges and scarps are labelled in the figure.

Figure 9: Variance slices across MTDa, Zone A. (a) Cariance slice of the flattened top of MTDa. (b) Variance slice 30 ms below the flattened top of MTDa. (c) Variance slice 30 ms above the flattened base of MTDa. (d) Variance slice of the flattened base of MTDa. Blocks, linear structures and scarps are identified in the figures.

Figure 10: Variance slice highlighting the internal character of MTDs in Zone B. (a) Variance slice of the flattened base of MTDb1. (b) Variance slice of the flattened base of MTDb2. (c) Variance slice of the flattened base of MTDb6. (d) Variance slice at a two-way time depth of 2850 ms, highlighting the distribution of free gas (dashed pink line) and MTDb5 and MTDb6 at this depth. Blocks and grooves are identified and indicates that MTDs were transported from NW to SE.

Figure 11: Isochron thickness map of MTDb1, Zone B. MTDb1 is shown to pinch out towards the southern part of the

study area.

Figure 12: Relative distribution of MTDb1 to MTDb6 and free gas in Zone B. The main volume of free gas is overlain by MTDb5 and MTDb6.

Figure 13: Well log data from (a) IODP Site 1323 and (b) ODP Site 936A highlighting the petrophysical character of MTDs at these locations after their emplacement. The water content and porosity of MTDs decrease, whereas the density, compressional velocity and resistivity increase after their emplacement. This indicates that the MTDs are more consolidated strata above and below, and form competent seal intervals.

Figure 14: Conceptual models for fluid migration and accumulation underneath MTDs in Zone A (a) and Zone (b). In Zone A, vertical fluid migration chiefly occurs by diffusion along porous strata. After the fluid reaches the base of MTDa is trapped by overconsolidated strata in this deposit, and migrates laterally along its base. In Zone B, vertical fluid migration chiefly occurs via gas chimneys and pipes. Fluid is trapped by MTDb5 and MTDb6 and accumulates within porous strata below the two MTDs, particularly in their basal shear zones.

Table caption

Table 1: Geometric characteristics of MTDs and free gas in Zones A and B. AT = average thickness; MTD = Mass-transport deposit. Please note that the average thickness and volume of free gas reflect the thickness and volume of gas-bearing strata in the two studied zones. ∗ means a conservative value.

Figure 1

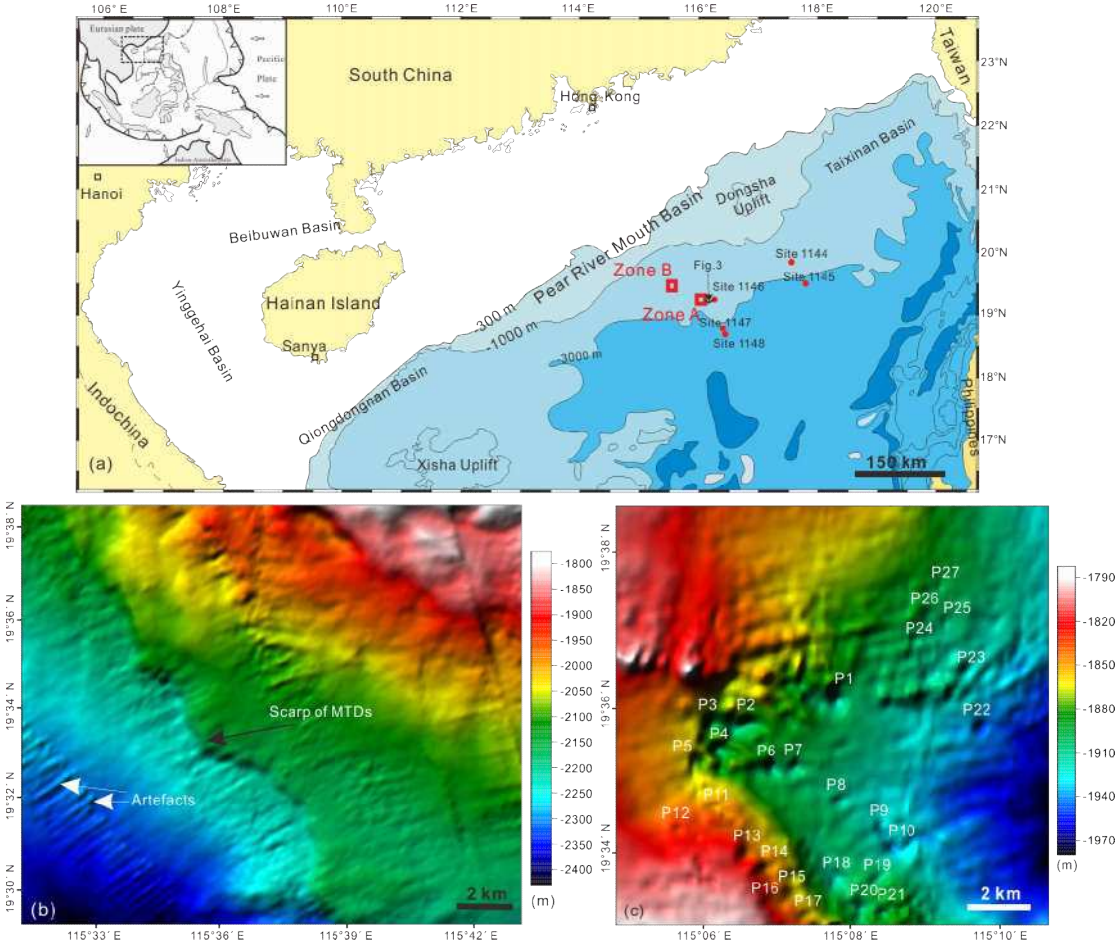
106° E
108°E
110°E
112°E
114°E
116°E
118°E
120°E
23°N
22°N
21°N
20°N
19°N
18°N
17°N
South China
Hong Kong
Taiwan
Hanoi
Beibuwan Basin
Pear River Mouth Basin
Dongsha Uplift
Taixinan Basin
Zone B
Fig.3
Site 1144
Site 1145
Site 1146
Zone A
Site 1147
Site 1148
Hainan Island
Sanya
Yinggehai Basin
300 m
1000 m
3000 m
Qiongdongnan Basin
Indochina
Xisha Uplift
Philippines
(a)
150 km
19°38´ N
19°36´ N
19°34´ N
19°32´ N
19°30´ N
Scarp of MTDs
Artefacts
2 km
(b)
115°33´ E
115°36´ E
115°39´ E
115°42´ E
-1800
-1850
-1900
-1950
-2000
-2050
-2100
-2150
-2200
-2250
-2300
-2350
-2400
(m)
P27
P26
P25
P24
P23
P1
P3
P2
P22
P4
P5
P6
P7
P8
P11
P12
P9
P10
P13
P14
P18
P19
P15
P16
P17
P20
P21
2 km
(c)
115°06´ E
115°08´ E
115°10´ E
-1790
-1820
-1850
-1880
-1910
-1940
-1970
(m)

Figure 2

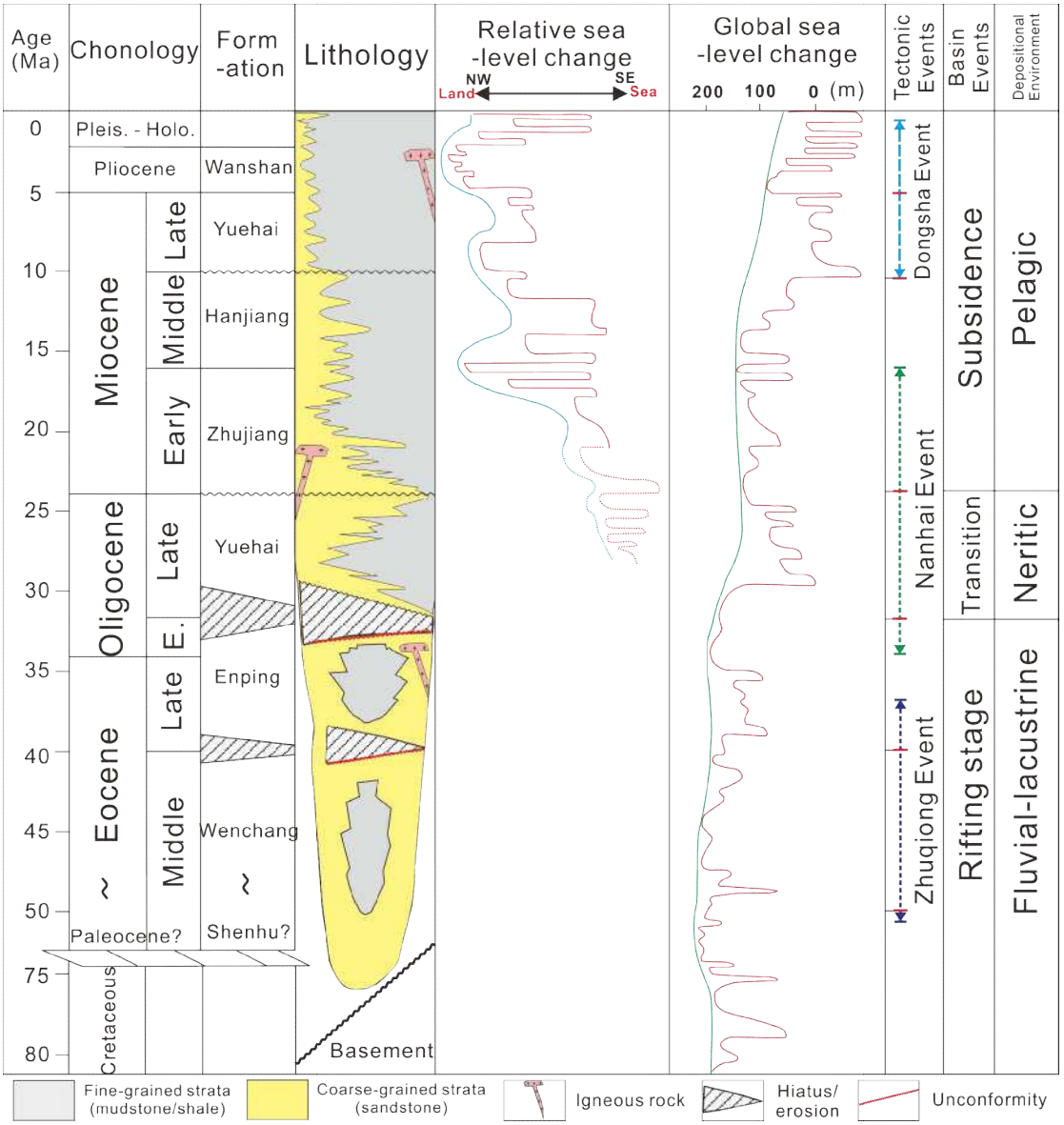
Age (Ma)
Chonology
Form -ation
Lithology
Relative sea -level change
NW
Land
SE
Sea
Global sea -level change
200
100
0 (m)
Tectonic Events
Basin Events
Depositional Environment
0
5
10
15
20
25
30
35
40
45
50
75
80
Pleis. - Holo.
Pliocene
Miocene
Late
Middle
Early
Oligocene
Late
E.
Eocene
~
Late
Middle
Paleocene?
Cretaceous
Wanshan
Yuehai
Hanjiang
Zhujiang
Yuehai
Enping
Wenchang
~
Shenhu?
Basement
Dongsha Event
Nanhai Event
Zhuqiong Event
Subsidence
Transition
Rifting stage
Pelagic
Neritic
Fluvial-lacustrine
Fine-grained strata (mudstone/shale)
Coarse-grained strata (sandstone)
Igneous rock
Hiatus/ erosion
Unconformity

Figure 3

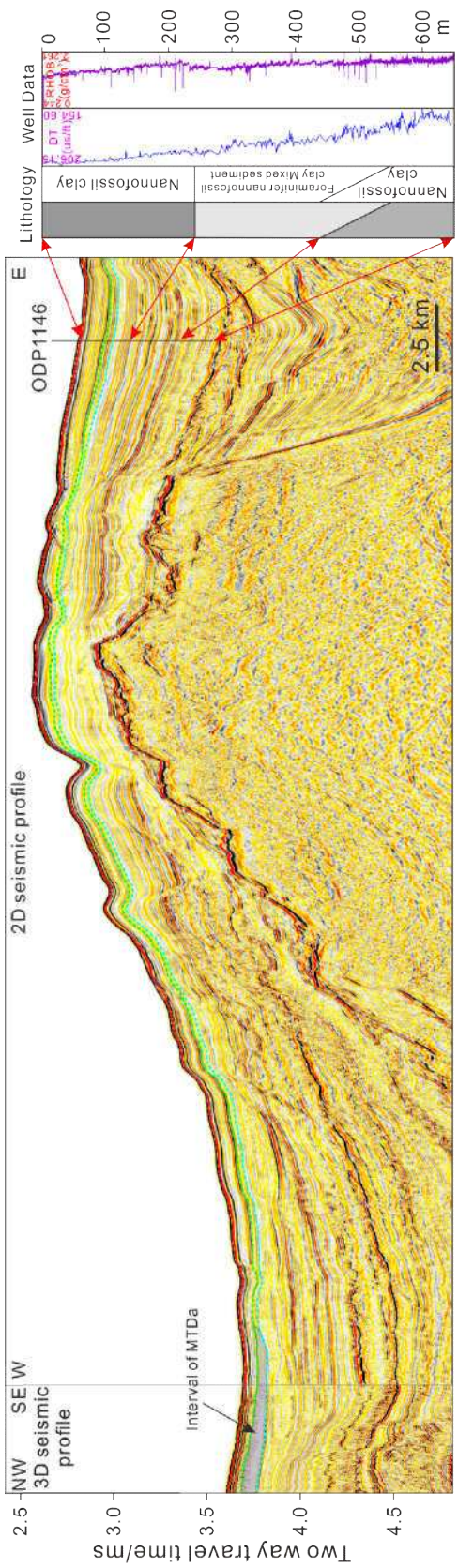
Lithology
Well Data
Nannofossil clay
Foraminifer nannofossil clay Mixed sediment
Nannofossil clay
0
100
200
300
400
500
600
m
E
ODP1146
2.5 km
2D seismic profile
NW
SE
W
3D seismic profile
Interval of MTDa
2.5
3.0
3.5
4.0
4.5
Two way travel time/ms

Figure 4

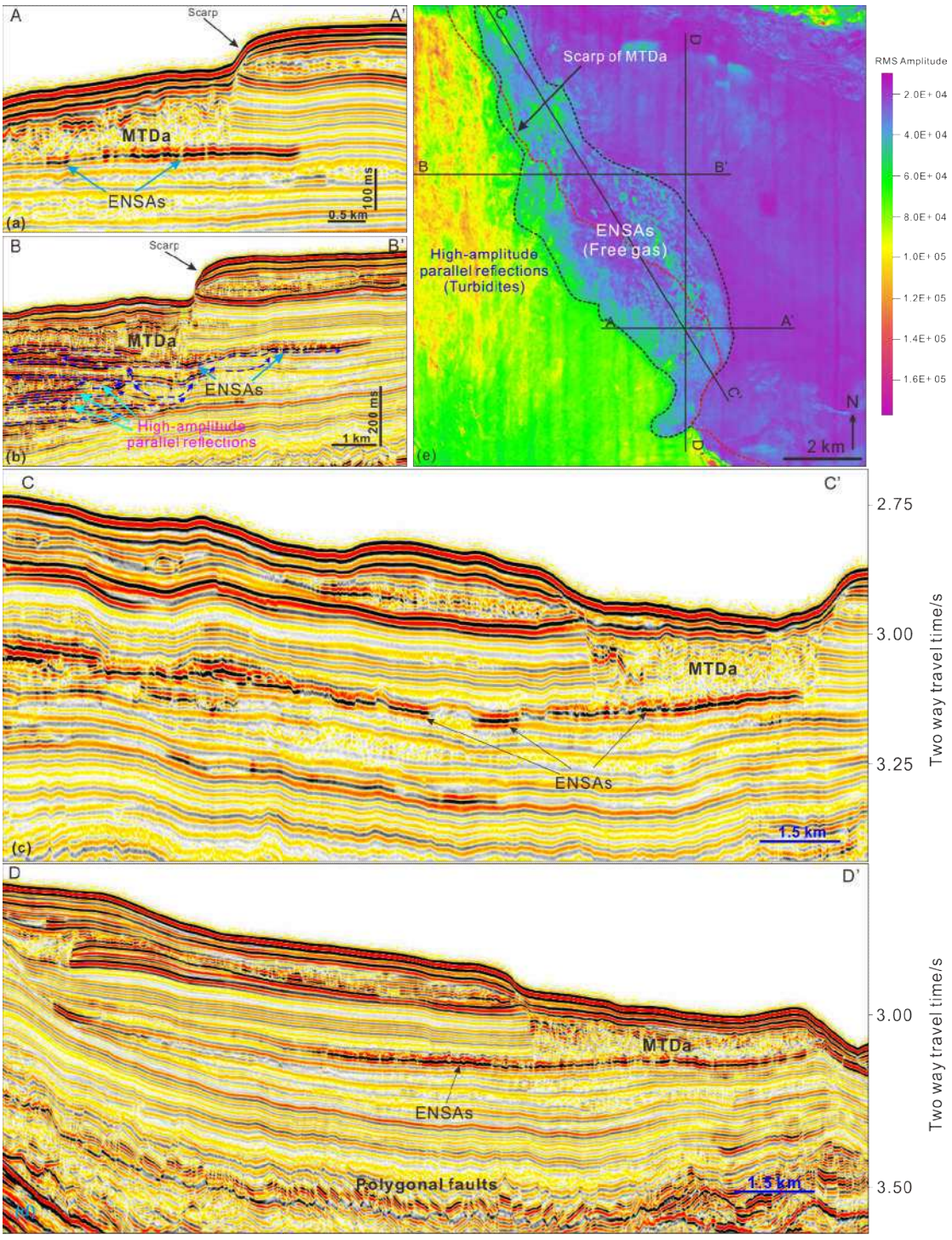
A
A'
Scarp
MTDa
ENSAs
100 ms
0.5 km
(a)
B
B'
Scarp
MTDa
ENSAs
High-amplitude
parallel reflections
200 ms
1 km
(b)
Scarp of MTDa
ENSAs
(Free gas)
High-amplitude
parallel reflections
(Turbidites)
2 km
N
(e)
RMS Amplitude
2.0E+04
4.0E+04
6.0E+04
8.0E+04
1.0E+05
1.2E+05
1.4E+05
1.6E+05
C
C'
MTDa
ENSAs
1.5 km
(c)
2.75
3.00
3.25
Two way travel time/s
D
D'
MTDa
ENSAs
Polygonal faults
1.5 km
(d)
3.00
3.50
Two way travel time/s

Figure 5

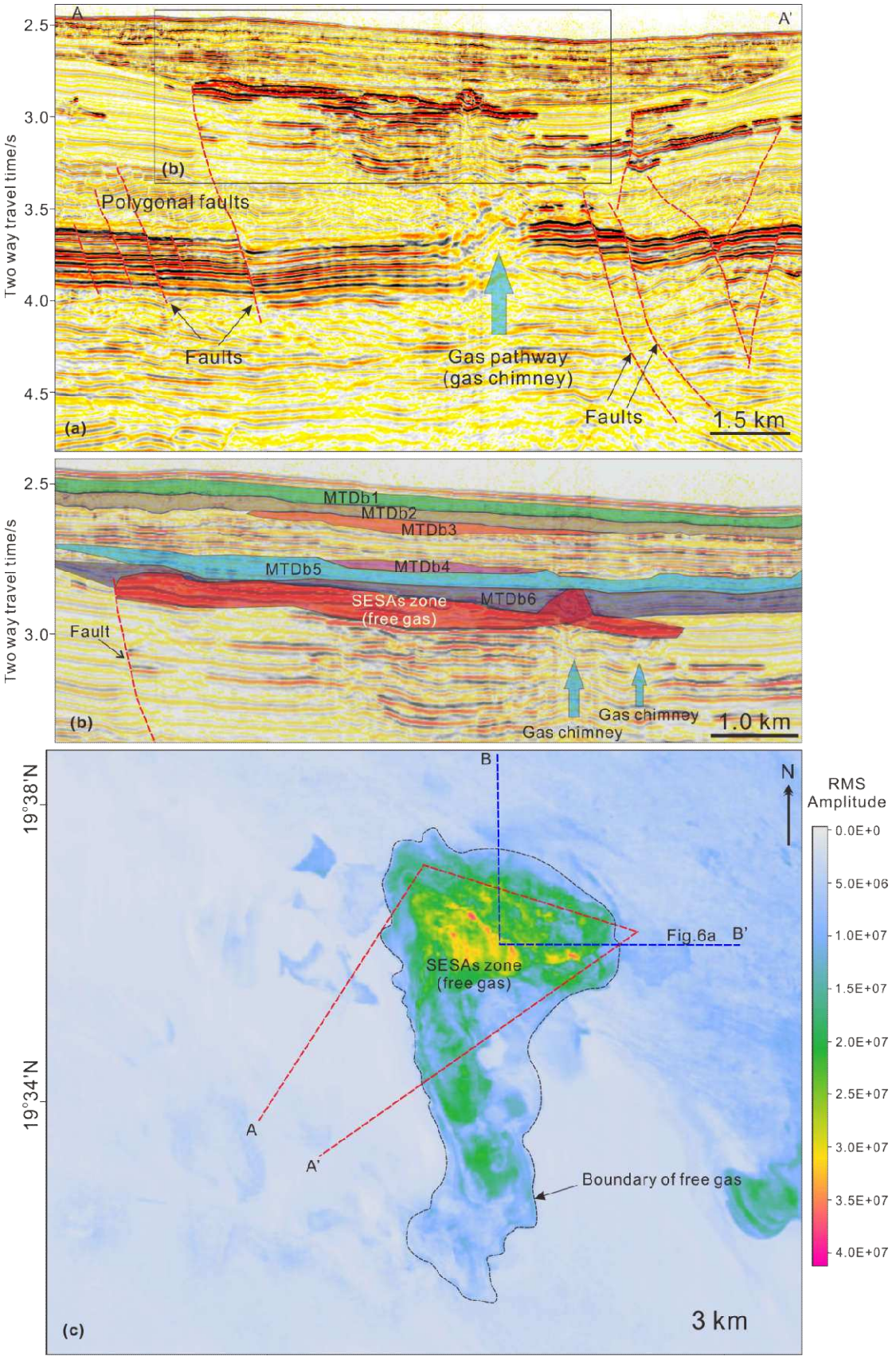
A
A'
(b)
Polygonal faults
Faults
Gas pathway
(gas chimney)
Faults
1.5 km
(a)
Two way travel time/s
2.5
3.0
3.5
4.0
4.5
MTDb1
MTDb2
MTDb3
MTDb5
MTDb4
SESAs zone
(free gas)
MTDb6
Fault
Gas chimney
Gas chimney
1.0 km
(b)
B
N
RMS
Amplitude
0.0E+0
5.0E+06
1.0E+07
1.5E+07
2.0E+07
2.5E+07
3.0E+07
3.5E+07
4.0E+07
Fig.6a
B'
SESAs zone
(free gas)
A
A'
Boundary of free gas
19°38'N
19°34'N
3 km
(c)

Figure 6

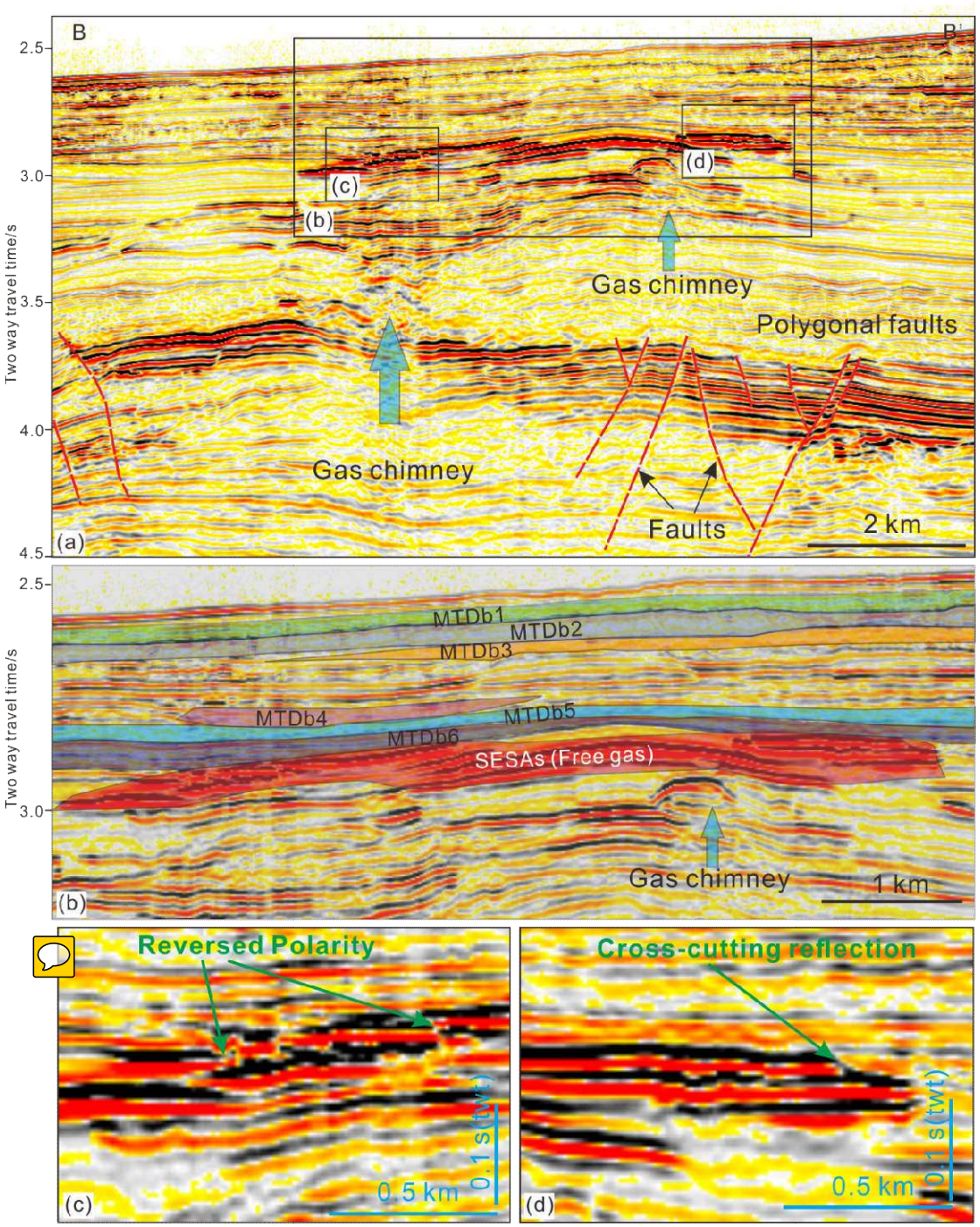
B
B'
2.5
3.0
3.5
4.0
4.5
Two way travel time/s
(c)
(b)
(d)
Gas chimney
Polygonal faults
Gas chimney
Faults
2 km
(a)
MTDb1
MTDb2
MTDb3
MTDb4
MTDb5
MTDb6
SESAs (Free gas)
Gas chimney
1 km
(b)
Reversed Polarity
0.1 s (twt)
0.5 km
(c)
Cross-cutting reflection
0.1 s (twt)
0.5 km
(d)

Figure 7

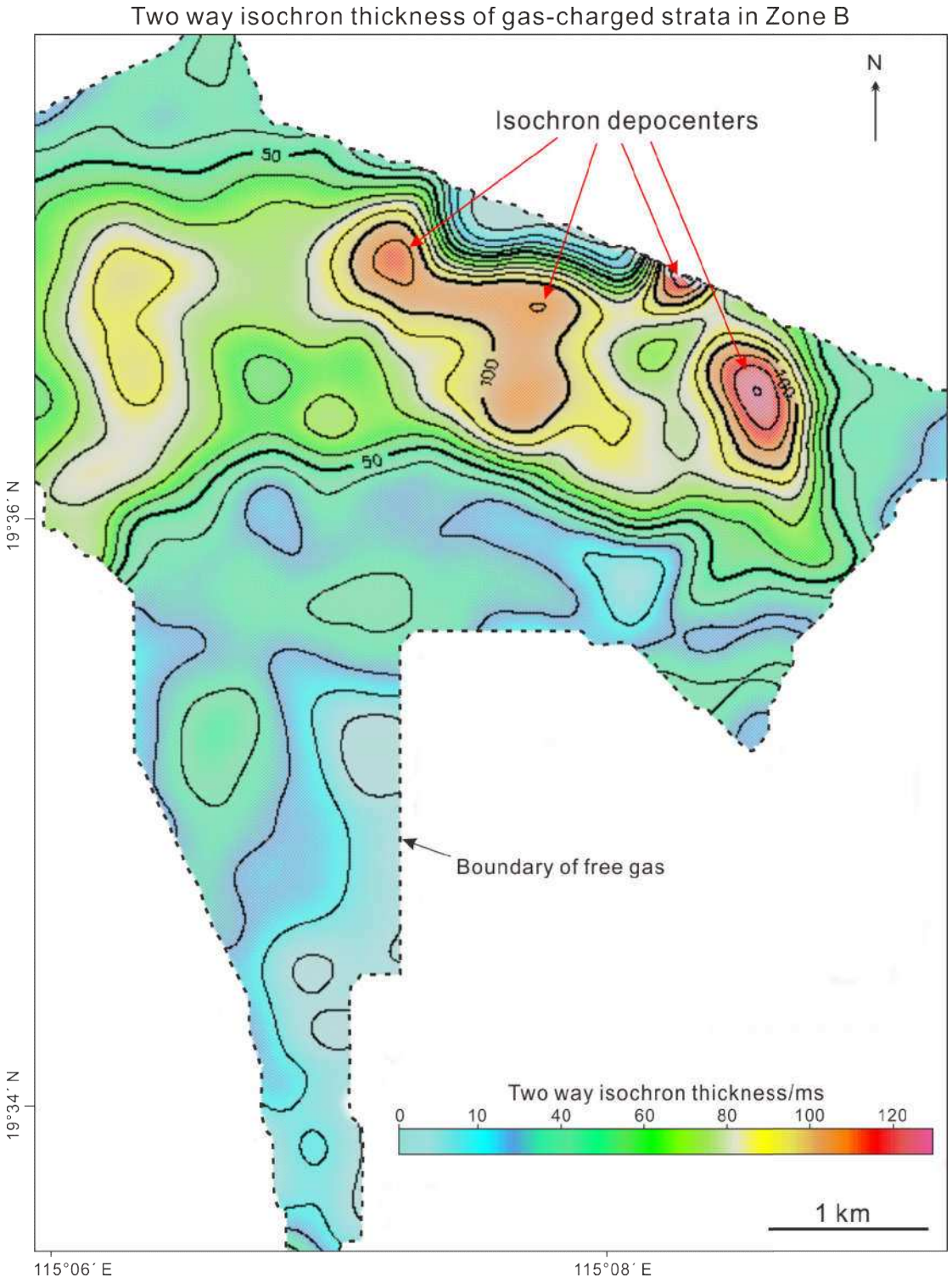
Two way isochron thickness of gas-charged strata in Zone B
N
Isochron depocenters
50
100
150
50
Boundary of free gas
19°36′ N
19°34′ N
Two way isochron thickness/ms
0
10
40
60
80
100
120
1 km
115°06′ E
115°08′ E

Figure 8

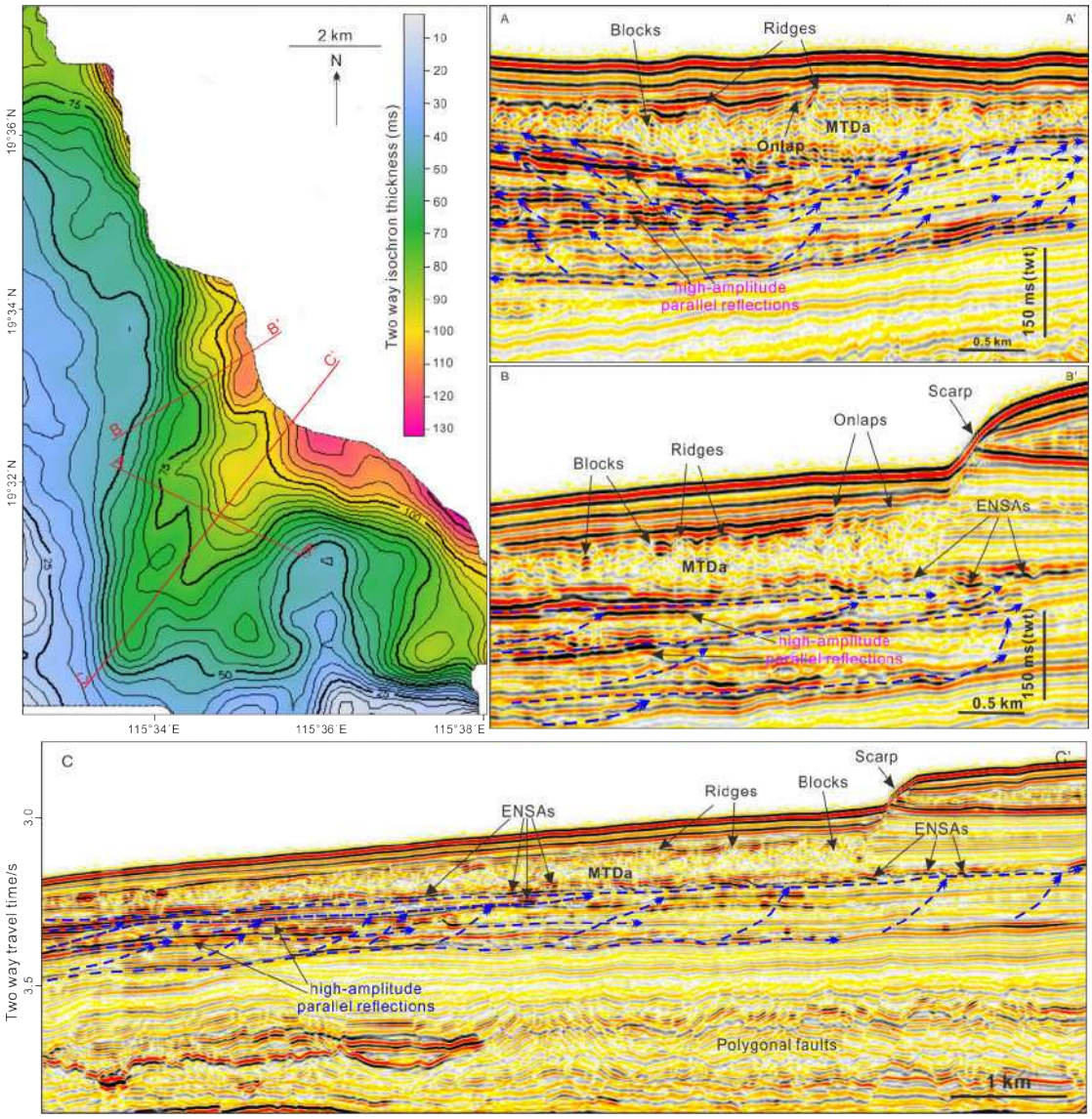
2 km
N
Two way isochron thickness (ms)
19°36'N
19°34'N
19°32'N
115°34'E
115°36'E
115°38'E
A
A'
Blocks
Ridges
MTDa
Onlap
high-amplitude
parallel reflections
150 ms(twt)
0.5 km
B
B'
Scarp
Onlaps
Blocks
Ridges
ENSAs
MTDa
high-amplitude
parallel reflections
150 ms(twt)
0.5 km
C
C'
Scarp
Ridges
Blocks
ENSAs
ENSAs
MTDa
high-amplitude
parallel reflections
Polygonal faults
1 km
Two way travel time/s
3.0
3.5

Figure 9

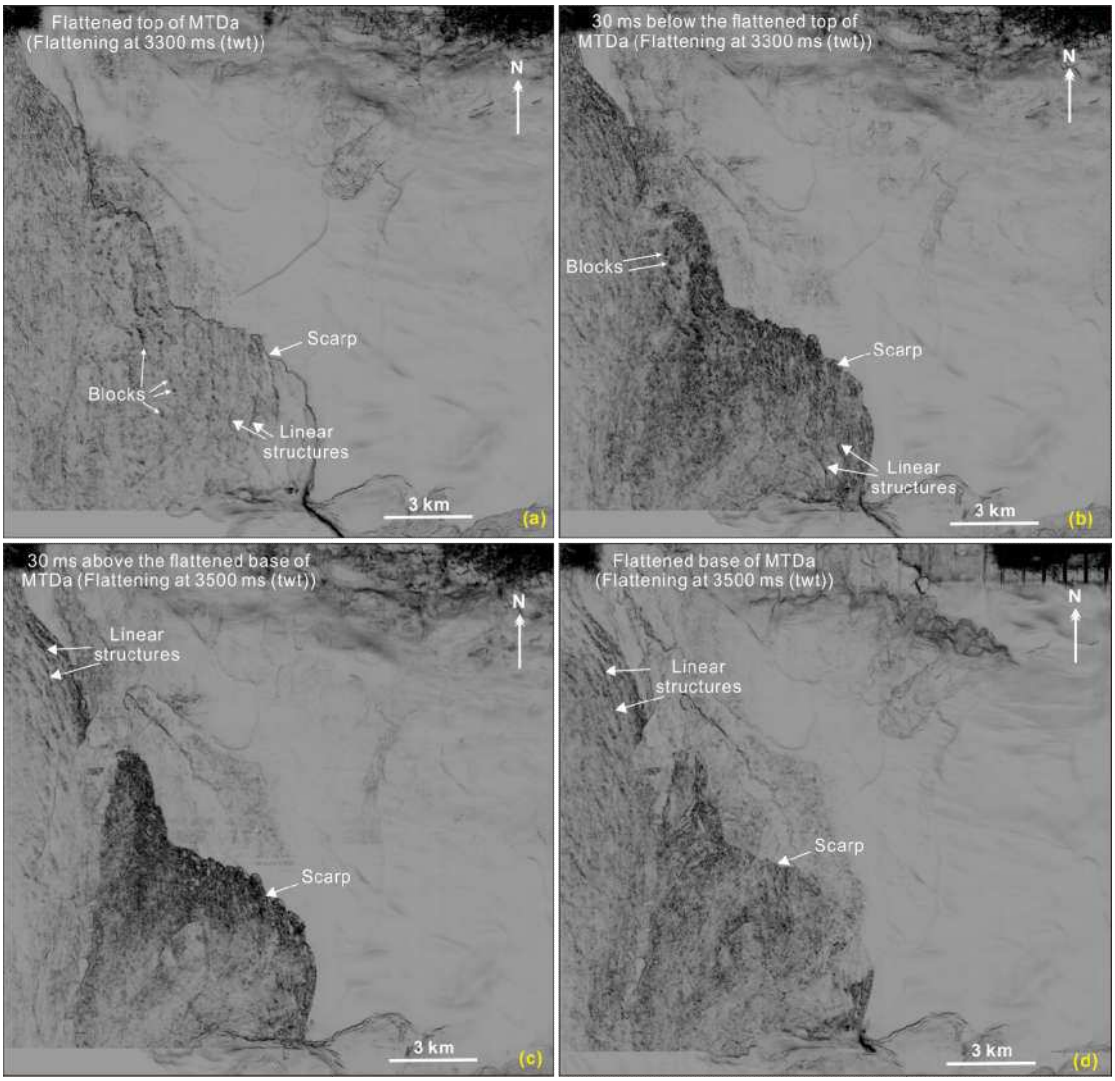
Flattened top of MTDa
(Flattening at 3300 ms (twt))
N
Scarp
Blocks
Linear
structures
3 km
(a)
30 ms below the flattened top of
MTDa (Flattening at 3300 ms (twt))
N
Blocks
Scarp
Linear
structures
3 km
(b)
30 ms above the flattened base of
MTDa (Flattening at 3500 ms (twt))
N
Linear
structures
Scarp
3 km
(c)
Flattened base of MTDa
(Flattening at 3500 ms (twt))
N
Linear
structures
Scarp
3 km
(d)

Figure 10

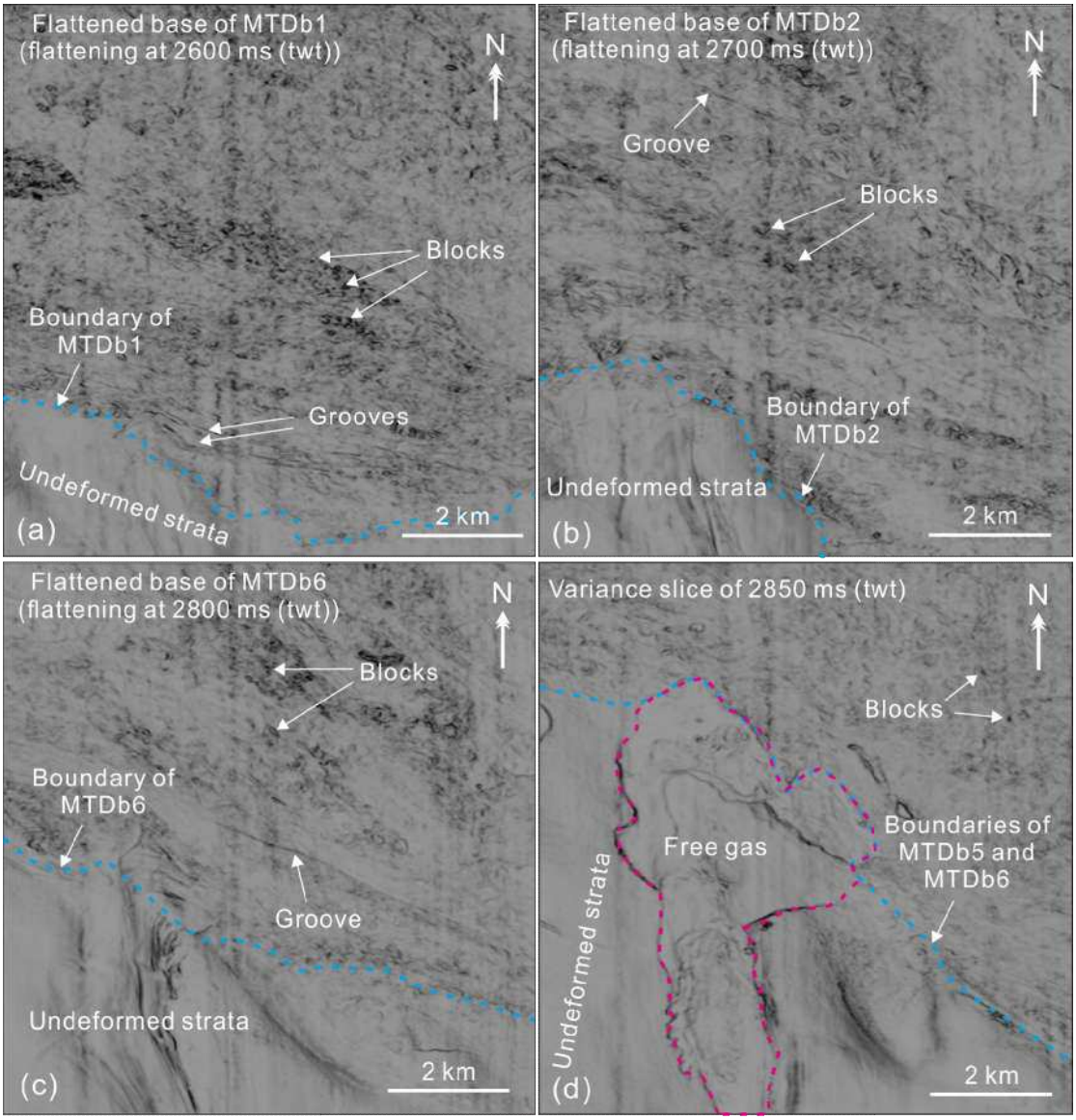
Flattened base of MTDb1
(flattening at 2600 ms (twt))
N
Blocks
Boundary of
MTDb1
Grooves
Undeformed strata
2 km
(a)
Flattened base of MTDb2
(flattening at 2700 ms (twt))
N
Groove
Blocks
Boundary of
MTDb2
Undeformed strata
2 km
(b)
Flattened base of MTDb6
(flattening at 2800 ms (twt))
N
Blocks
Boundary of
MTDb6
Groove
Undeformed strata
2 km
(c)
Variance slice of 2850 ms (twt)
N
Blocks
Free gas
Boundaries of
MTDb5 and
MTDb6
Undeformed strata
2 km
(d)

Figure 11

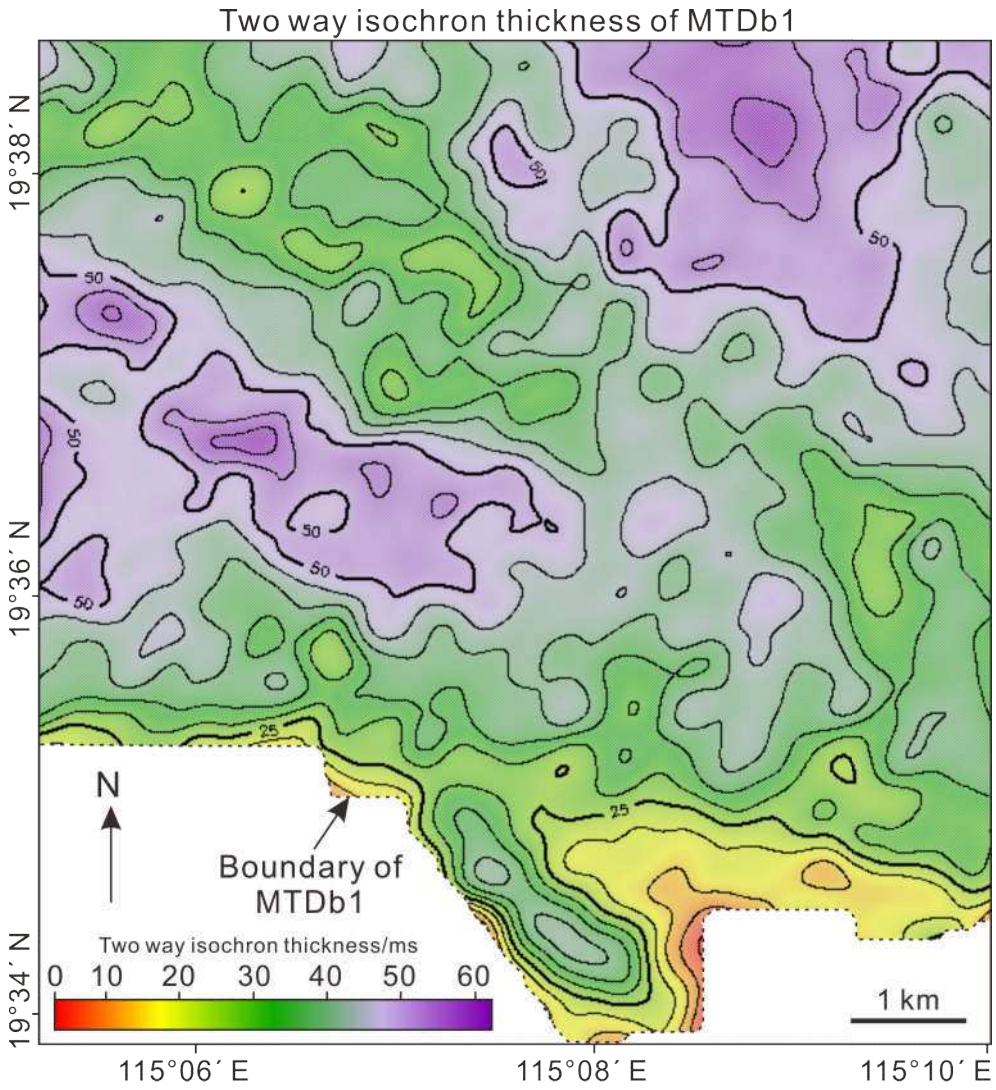
Two way isochron thickness of MTDb1
19°38´ N
19°36´ N
19°34´ N
115°06´ E
115°08´ E
115°10´ E
N
Boundary of MTDb1
Two way isochron thickness/ms
0 10 20 30 40 50 60
1 km
50
25

Figure 12

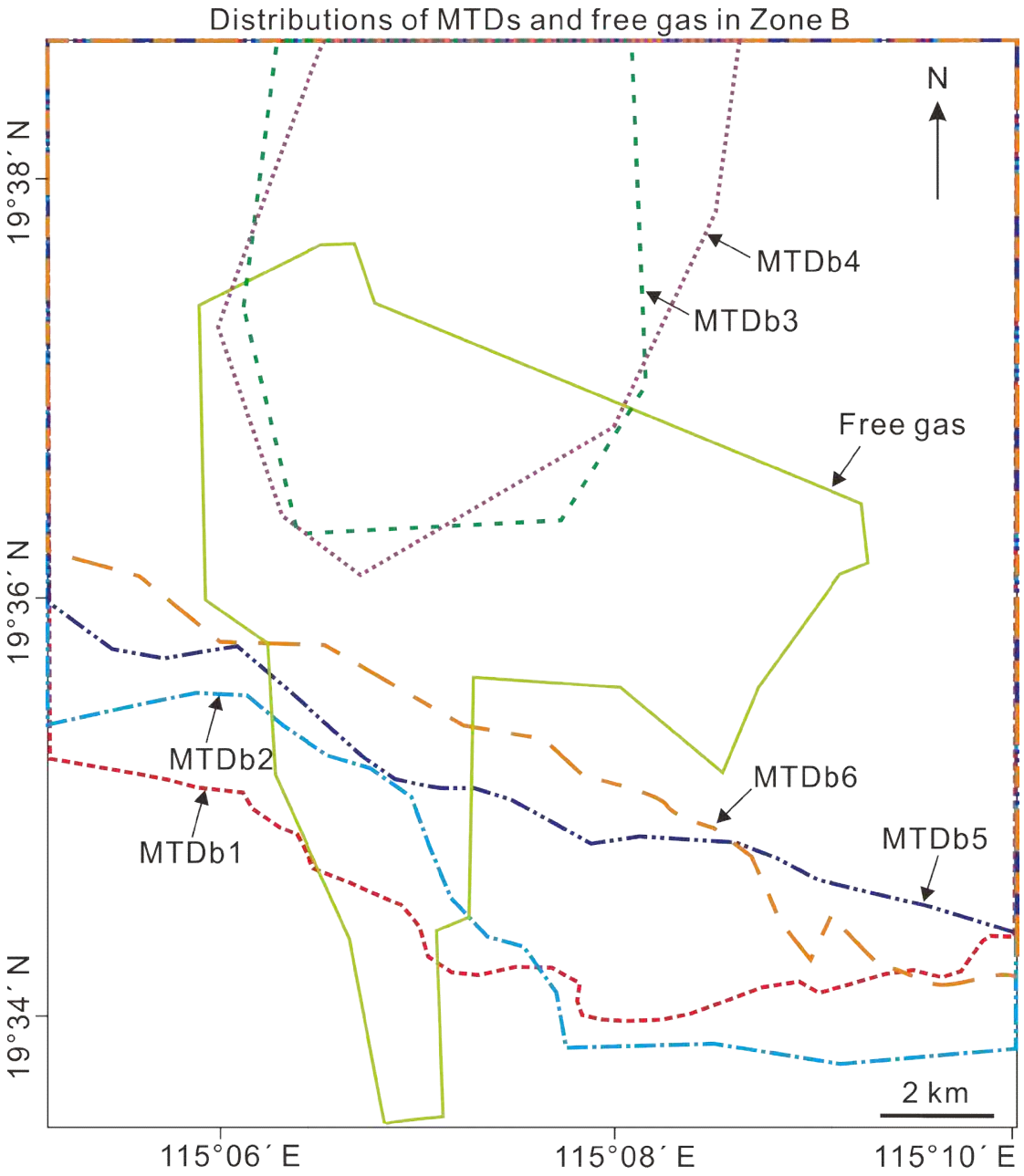
Distributions of MTDs and free gas in Zone B
N
MTDb4
MTDb3
Free gas
MTDb2
MTDb1
MTDb6
MTDb5
2 km
19°38′ N
19°36′ N
19°34′ N
115°06′ E
115°08′ E
115°10′ E

Figure 13

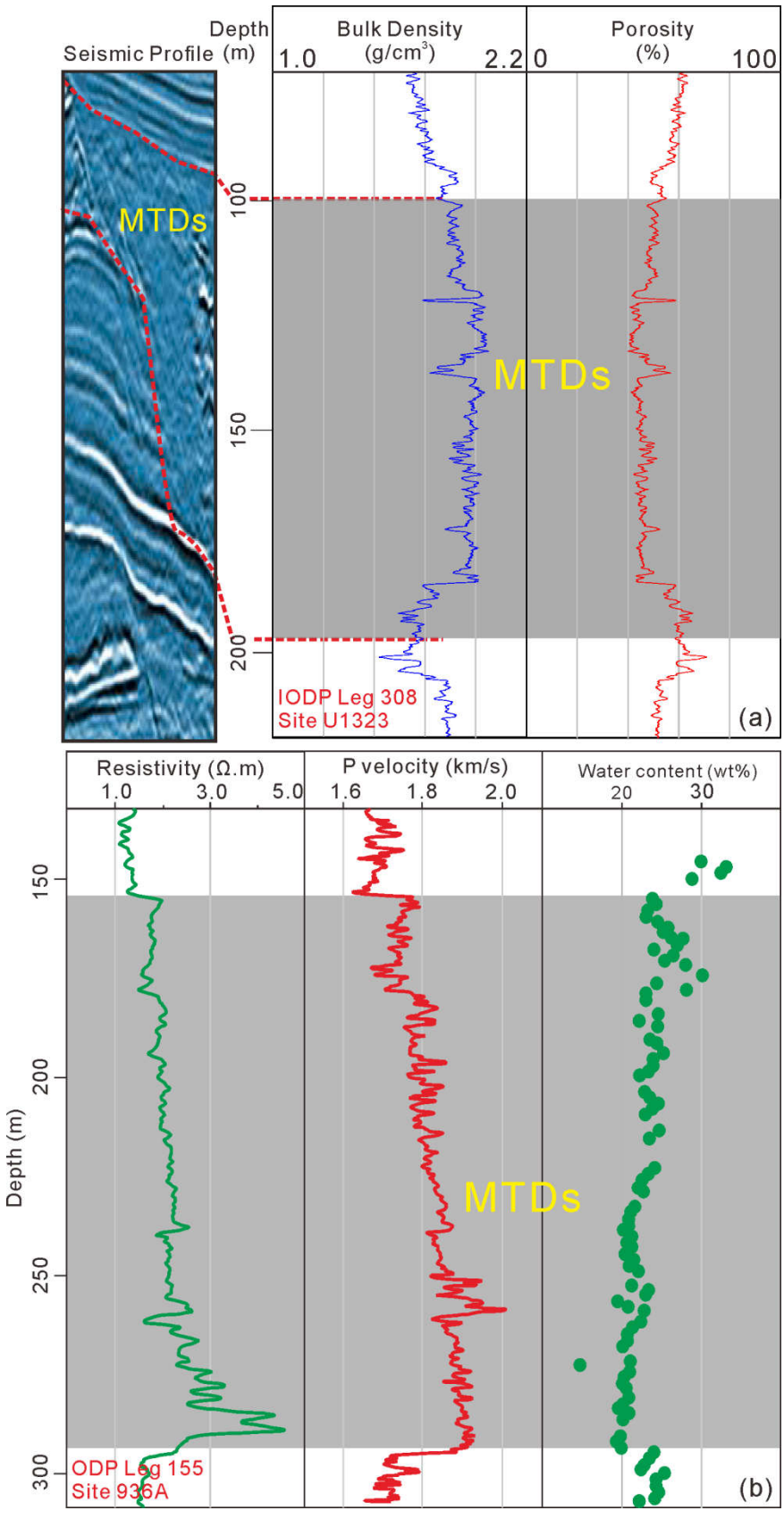
Depth
Seismic Profile (m)
Bulk Density
(g/cm3)
1.0
2.2
Porosity
(%)
0
100
MTDs
100
150
200
MTDs
IODP Leg 308
Site U1323
(a)
Resistivity (Ω.m)
1.0
3.0
5.0
P velocity (km/s)
1.6
1.8
2.0
Water content (wt%)
20
30
Depth (m)
150
200
250
300
MTDs
ODP Leg 155
Site 936A
(b)

Figure 14

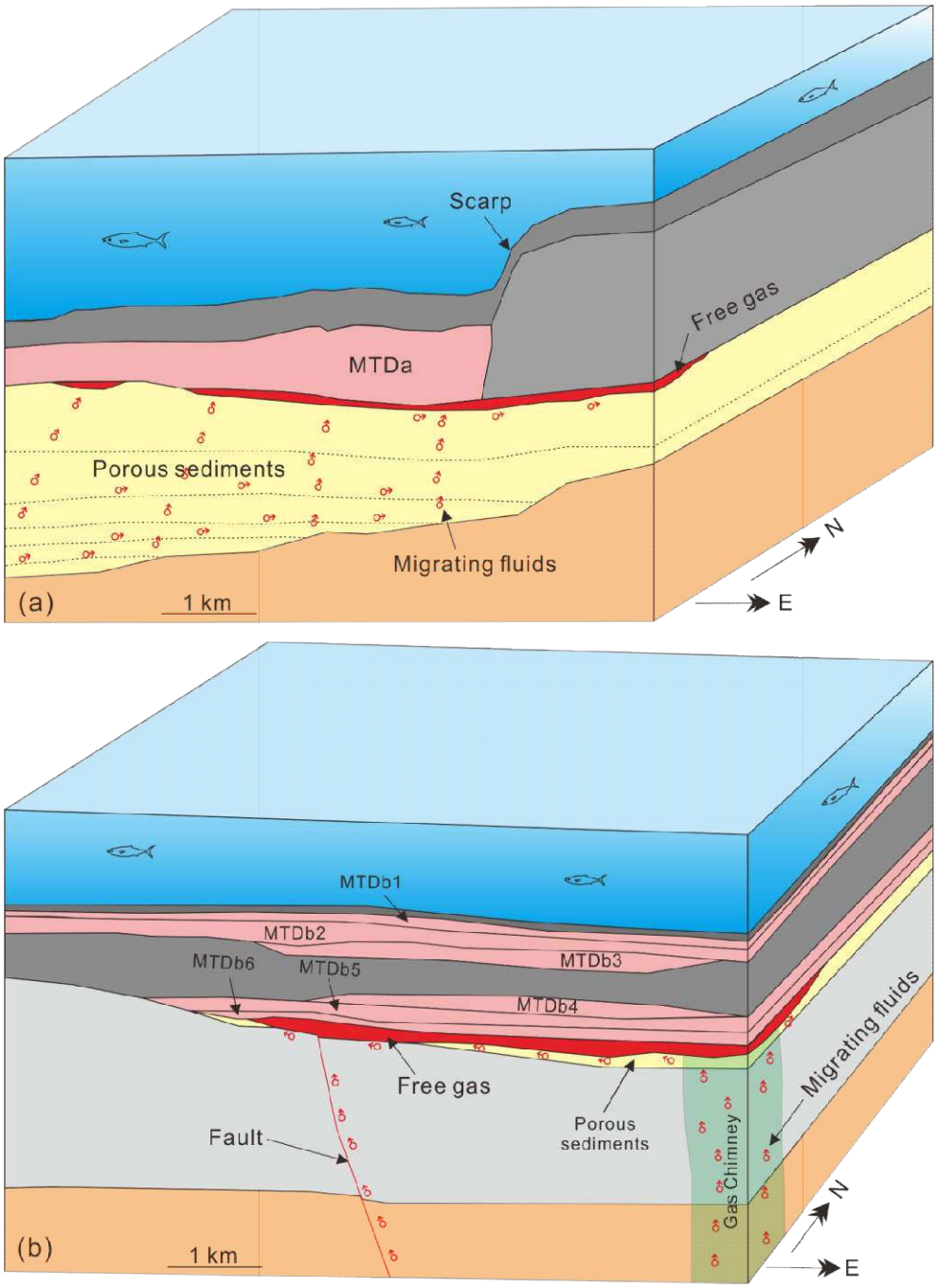
Scarp
Free gas
MTDa
Porous sediments
Migrating fluids
(a)
1 km
N
E
MTDb1
MTDb2
MTDb3
MTDb4
MTDb5
MTDb6
Free gas
Fault
Porous sediments
Gas Chimney
Migrating fluids
(b)
1 km
N
E